Journal of Computational Physics 228 (2009) 3762–3788

Contents lists available at ScienceDirect

Journal of Computational Physics

journal homepage: www.elsevier.com/locate/jcp

Towards a compact high-order method for non-linear hyperbolic systems. I: The Hermite Least-Square Monotone (HLSM) reconstruction

G. Capdeville *

Département de Mecanique des Fluides, Ecole Centrale de Nantes, 1, rue de la Noë, B.P. 92101, 44321 Nantes cedex 3, France

ARTICLE INFO

Article history:
Received 8 February 2008
Received in revised form 9 January 2009
Accepted 6 February 2009
Available online 14 February 2009

Keywords:
Least-square reconstruction
Hermite polynomial
Data-depending weight
Hyperbolic systems
Non-uniform meshes
Upwind discretization
Aero-acoustics

ABSTRACT

A new Hermite Least-Square Monotone (HLSM) reconstruction to calculate accurately complex flows on non-uniform meshes is presented.

The coefficients defining the Hermite polynomial are calculated by using a least-square method. To introduce monotonicity conditions into the procedure, two constraints are added into the least-square system. Those constraints are derived by locally matching the high-order Hermite polynomial with a low-order TVD or ENO polynomial. To emulate these constraints only in regions of discontinuities, data-depending weights are defined; those weights are based upon normalized indicators of smoothness of the solution and are parameterized by a $O(1)$ quantity. The reconstruction so generated is highly compact and is fifth-order accurate when the solution is smooth; this reconstruction becomes first-order in regions of discontinuities.

By inserting this reconstruction into an explicit finite-volume framework, a spatially fifth-order non-oscillatory method is then generated. This method evolves in time the solution and its first derivative. In a one-dimensional context, a linear spectral analysis and extensive numerical experiments make it possible to assess the robustness and the advantages of the method in computing multi-scales problems with embedded discontinuities.

1. Introduction

Nowadays, there is a growing need for high-order numerical methods in Computational Fluid Dynamics (CFD). Aero acoustics, turbulence modelling or magneto hydrodynamics are domains for which high-order accuracy is strongly needed. Flow problems with intricate structures and a broad range of characteristic scales cannot be efficiently modelled by conventional second-order numerical methods; even on very fine meshes, those methods are unable to correctly extract a weak signal from the mean flow.

Relying on a finite-volume framework, the definition of a reconstruction procedure of the solution from its cell-averaged values is the first important task in obtaining a high-order numerical method.

Ideally, the reconstruction should ensure high-order accuracy, even on non-Cartesian meshes, while preserving the monotonicity of the solution.

Starting from the pioneering work of Van-Leer in 1977 [1] much work was done on this topic. In 1987, Harten et al. developed the henceforth-classic category of essentially non-oscillatory schemes (ENO) [2]. Later, Liu et al. [3] improved ENO schemes by developing the class of weighted essentially non-oscillatory (WENO) schemes (see [4] for a good overview on these methods).

* Tel.: +33 2 4037 1651; fax: +33 2 4037 2523.
E-mail address: guy.capdeville@ec-nantes.fr

0021-9991/$ - see front matter © 2009 Elsevier Inc. All rights reserved.
doi:10.1016/j.jcp.2009.02.005

However, in spite of their vast field of application, standard WENO schemes still have deficiencies: due to the width of their numerical stencil, the extension to non-Cartesian meshes is somewhat cumbersome; moreover, a wide stencil is not optimum neither in terms of an accurate treatment of weak fluctuations, nor concerning the imposition of boundary conditions. Considering those limits, a possibility is to introduce more information of the numerical solution in the neighbourhood of any given cell. Recently, Liu [19] proposed a solution by using an overlapping cell representation of the solution with two sets of cell averages; doing this way, a compact reconstruction to achieve higher resolution, was possible. Instead of using overlapping cells, another solution is to consider the solution proposed by the class of CIP/multi-moment finite volume method [20] in which the conservative variable is computed through a flux-form formulation and a non-conservative moment (first derivative or point-value) by a semi Lagrangian procedure.

In a previous work, we developed a new class of WENO schemes based on a convex combination of Hermite polynomials [5]. On a one-dimensional basis and following the original WENO philosophy, the solution and its first derivative are evolved in time and used into the polynomial reconstruction. With a three-points numerical stencil, we demonstrated that this procedure generates a sixth-order scheme (in terms of truncature error) in smooth regions and for small CFLs. Furthermore, a new formulation of the non-linear weights used in the convex combination, enables to generate a non-linearly stable reconstruction near discontinuities. The resulting scheme becomes of the fourth-order in the cells close to the discontinuity and can even become first-order at the location of the discontinuity if the Hermite interpolation is potentially oscillatory. Compared to the class of CIP schemes, the extra-moment is now effectively updated through a finite-volume formulation of flux form, and therefore is numerically conserved. Maintaining these design principles, such a method can be straightforwardly extended to multi-dimensional problems. This can be achieved by simply applying a Hermite reconstruction, direction-by-direction.

Such a choice is valid as long as the mesh remains Cartesian or, at least, is smoothly varying. When this is no more the case, the formal accuracy of the scheme, and its associated advantages, are largely lost. Moreover, the cross-derivatives of the solution are not at all calculated: this necessitates refining exaggeratedly the mesh when rapid variations of the solution are not aligned with the local grid directions.

Accordingly, we propose in this article a new approach that is designed to be compatible with multi-dimensional extensions on non-Cartesian mesh. To preserve the compactness of the stencil, this approach still relies upon Hermite polynomials; however, these polynomials are now constructed by a least square methodology.

The use of a least-square reconstruction to build a high-order finite-volume scheme is not a novelty. A few years ago, Barth [6,7] produced a great amount of work on this subject. He constructed an upwind finite-volume scheme, via a Godunov's method, to be utilized on unstructured meshes. In the reconstruction step, Barth devised a least-square method to calculate the polynomial coefficients. The reconstruction could be either linear (second-order accuracy in smooth regions; see [6] for details) or quadratic (third-order accuracy [7]). To enforce monotonicity in regions of discontinuities, the piecewise linear (or quadratic) distribution of the solution in each cell was "limited" by using a specific limiter. The resulting scheme proved to be highly successful on a large variety of problems, even on highly distorted unstructured meshes.

In [6], Barth gave general indications to construct a least-square method including data-dependent weights. However, he did not develop such a possibility into his paper. This is the merit of Ollivier-Gooch to have concretized this idea [8].

Ollivier-Gooch devises a least-square reconstruction scheme suitable for use on unstructured meshes and modifies it to satisfy the ENO property. This modification is ensured by a data-dependent weighting that uses the residual of the least-square problem - to detect stencils with non-smooth data – and the local gradient of the solution – to determine which data within that stencil should be excluded – (see [8] for details). This way, the resulting scheme ("DD-L2-ENO" scheme) is demonstrated to be uniformly accurate, even in the presence of discontinuities, and allows only asymptotically small overshoots.

However, as Ollivier-Gooch states it in his article, such a scheme is not designed to produce high-order accurate solutions: required stencils sizes for such high-accuracy grow very rapidly; in other words, the numerical stencil is not enough compact. Moreover, this procedure necessitates to solve two least-square problems. Indeed, a least-square problem is first necessary to evaluate the residual and then to calculate data-dependent weights; a second least-square problem, modified by those weights, is then solved to give the derivatives needed by the reconstruction. This feature results in a very costly method, especially when this procedure is used for systems.

Considering the work of Barth and Ollivier-Gooch, our point of view is different: instead of constructing a polynomial and then, to modify it in order to preserve the monotonicity, we introduce a monotonicity principle *into* the calculation of the polynomial coefficients. This is achieved by using a least-square method with specific additional constraints.

Keeping in mind the necessary compactness of the discretization and capitalizing on the experience gained in [5], the method we developed has the following features:

- A Hermite polynomial reconstruction using the solution and its first derivative is devised. The numerical stencil is selected so as the interpolated solution using this reconstruction, is fifth-order accurate – in terms of truncature error – in regions of smoothness.
- We utilize a least-square methodology to calculate the polynomial coefficients. When solved without any modification, the resulting system generates a fifth-order approximation in regions of smoothness and Gibbs-like phenomena in regions of discontinuities.

- To introduce a monotonicity condition into this reconstruction, we add two constraints to the initial system. Imposing that the oscillatory reconstruction locally coincides with a monotone reconstruction generates those constraints. This monotone reconstruction is obtained from a TVD or ENO condition.
- To emulate those constraints only in regions of discontinuities, we define a normalized smoothness indicator that is used to compute data-depending weights. Then, those weights are used to weight the constraints of monotonicity.

The result is a Hermite Least-Square Monotone (HLSM) reconstruction. Inserting this reconstruction into an upwind finite-volume formulation, we are able to devise a numerical scheme suited for computing multi-scales and non-linear problems, on irregular meshes.

This article is organized as follows: we start in Section 2 by defining the finite-volume framework of the method. In Section 3, we detail the construction and implementation of the HLSM reconstruction, for 1D scalar and 1D Euler equations. The interpolation polynomial is initially defined for use on irregular meshes; the specific procedure to generate a monotone reconstruction is then emphasized. To this end, we conceive a new second-order ENO interpolation, suited for a Hermite formulation: namely, the HENO2 reconstruction.

Finally, to have a first understanding of the capabilities of the method, we use a linear spectral analysis in Section 4. According to the magnitude of the data-depending weights, this analysis gives us the salient features of the method in terms of stability range, behaviour of the "spurious solution" and magnitude of the phase and amplitude errors. Technical details concerning this spectral analysis are given in Appendix.

Lastly, Section 5 presents numerical tests. Computed solutions of scalar non-linear and 1D Euler equations are presented and compared with WENO schemes, when necessary.

This work only concerns one-dimensional results.

2. Governing equations and finite-volume framework

2.1. Governing equations

Let the following scalar non-linear hyperbolic problem defined over the domain, Ω:

$$\begin{cases} u_t + f(u)_x = 0, \quad \forall x \in \Omega \\ u(x, t=0) = u_o(x) \end{cases} \tag{1}$$

Let $r \equiv u_x$ and $g(u,r) \equiv f'(u) \times u_x = f'(u) \times r$. Then by deriving (1), we can define the new non-linear hyperbolic problem over Ω:

$$\begin{cases} u_t + f(u)_x = 0, \quad u(x, t=0) = u_o(x) \\ r_t + g(u,r)_x = 0, \quad r(x, t=0) = u'_o(x) \end{cases} \tag{2}$$

Since $g(u,r) = f'(u) \times r$, this implies that the characteristic velocity, $\frac{\partial g}{\partial r}$, of the equation for the derivative variables, r, is $f'(u)$. Consequently, both equations constituting (2) share the same characteristic velocity: this result is used in what follows to generate a simple approximate Riemann solver discretizing (2). When the solution of (1) is discontinuous, system (2) is derived by using the newly developed theory of "delta-shock wave" (see [18] for details).

Defining the discrete cell $I_i \equiv [x_{i-1/2}, x_{i+1/2}]$, Ω is partitioned in N non-overlapping cells: $\Omega = \bigcup_{i=1}^{N} I_i$. The non-uniform cell size will be typified by: $\Delta x_i \equiv x_{i+1/2} - x_{i-1/2}$ or $\Delta x_{i+1/2} \equiv x_{i+1} - x_i$. Lastly, we define the discrete cell averages of $u(x,t)$ and $r(x,t)$ as: $\bar{u}_i(t) \equiv \frac{1}{\Delta x_i} \int_{I_i} u(x,t)dx$, $\bar{r}_i(t) \equiv \frac{1}{\Delta x_i} \int_{I_i} r(x,t)dx$. Integrating (2) over I_i produces the following system of ordinary differential equations (ODE) for the variables $\bar{u}_i, \bar{r}_i$:

$$\begin{cases} \frac{d\bar{u}_i}{dt} = -\frac{1}{\Delta x_i}[f(u(x_{i+1/2},t)) - f(u(x_{i-1/2},t))] \\ \frac{d\bar{r}_i}{dt} = -\frac{1}{\Delta x_i}[g(u(x_{i+1/2},t), r(x_{i+1/2},t)) - g(u(x_{i-1/2},t), r(x_{i-1/2},t))] \end{cases} \tag{3}$$

By using the classical "method of lines", time and space are separately discretized.

2.2. Spatial approximation: the numerical fluxes

Following the finite-volume methodology for generating a numerical scheme, the fluxes for $u$and r are approximated according to:

$$\begin{cases} f(u(x_{i+1/2},t)) \approx \tilde{f}_{i+1/2} \equiv \tilde{f}(u^L_{i+1/2}, u^R_{i+1/2}) \\ g(u(x_{i+1/2},t), r(x_{i+1/2},t)) \approx \tilde{g}_{i+1/2} \equiv \tilde{g}(u^L_{i+1/2}, r^L_{i+1/2}, u^R_{i+1/2}, r^R_{i+1/2}) \end{cases} \tag{4}$$

$u^{L,R}_{i+1/2}$ (resp. $r^{L,R}_{i+1/2}$) represent the numerical approximations to the point values $u(x_{i+1/2}, t_n)$ (resp. $r(x_{i+1/2}, t_n)$), Fig. 1. The way of constructing the numerical fluxes, $\tilde{f}, \tilde{g}$, defines the upwind method.

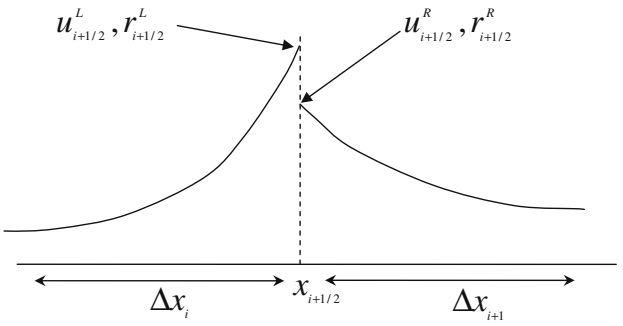

Fig. 1. Reconstruction of the point values from cell averages at the interface $x = x_{i+1/2}$.

To calculate those numerical fluxes, we selected the HLLE (Harten, Lax and Van-Leer) approximate Riemann solver [9]. Thus, we get the following expressions for the numerical fluxes $\tilde{f}$ and $\tilde{g}$:

$$\begin{cases} \tilde{f}_{i+1/2} = \frac{\lambda^+_{i+1/2} f(u^L_{i+1/2}) - \lambda^-_{i+1/2} f(u^R_{i+1/2})}{\lambda^+_{i+1/2} - \lambda^-_{i+1/2}} + \frac{\lambda^+_{i+1/2} \times \lambda^-_{i+1/2}}{\lambda^+_{i+1/2} - \lambda^-_{i+1/2}} (u^R_{i+1/2} - u^L_{i+1/2}) \\ \tilde{g}_{i+1/2} = \frac{\lambda^+_{i+1/2} g(u^L_{i+1/2}, v^L_{i+1/2}) - \lambda^-_{i+1/2} g(u^R_{i+1/2}, v^R_{i+1/2})}{\lambda^+_{i+1/2} - \lambda^-_{i+1/2}} + \frac{\lambda^+_{i+1/2} \times \lambda^-_{i+1/2}}{\lambda^+_{i+1/2} - \lambda^-_{i+1/2}} (v^R_{i+1/2} - v^L_{i+1/2}) \end{cases} \tag{5}$$

With, in the scalar case, the following choices for the characteristic velocities $\lambda^{\pm}_{i+1/2}$:

$$\begin{cases} \lambda^+_{i+1/2} \equiv \max(f'(u^L_{i+1/2}), f'(u^R_{i+1/2}), a_{i+1/2}, 0) \\ \lambda^-_{i+1/2} \equiv \min(f'(u^L_{i+1/2}), f'(u^R_{i+1/2}), a_{i+1/2}, 0) \end{cases} \tag{6}$$

$$\text{With} : a_{i+1/2} \equiv \begin{cases} (f(u^R_{i+1/2}) - f(u^L_{i+1/2}))/(u^R_{i+1/2} - u^L_{i+1/2}) & \text{if } u^R_{i+1/2} \neq u^L_{i+1/2} \\ f'(u^L_{i+1/2}) & \text{otherwise} \end{cases} \tag{7}$$

The discretization of the spatial operator generates an algebraic system of ODEs in time, for the discrete unknowns $(\bar{u}_i, \bar{r}_i)$. This system is integrated by using a third-order TVD Runge–Kutta scheme [12].

3. Hermite Least-Square Monotone (HLSM) reconstruction

In this section, we partly use notations introduced by Ollivier-Gooch in [8].

3.1. Least-square reconstruction from cell-averages $(\bar{u}_i, \bar{r}_i)$

To begin, we select an optimal Hermite polynomial of degree 4, denoted by $u_{opt}(x)$ and defined on the three-points stencil $\{I_{i-1}, I_i, I_{i+1}\}$, Fig. 2: $u_{opt}(x) \equiv \sum_{j=0}^{4} a_j (x - x_i)^j$.

Then, using the definition of $\bar{u}_i$:

$$\bar{u}_i \equiv \frac{1}{\Delta x_i} \int_{I_i} u_{opt}(x) dx = \frac{1}{\Delta x_i} \sum_{j=0}^{4} a_j \int_{I_i} (x - x_i)^j dx \tag{8}$$

and introducing the practical notation:

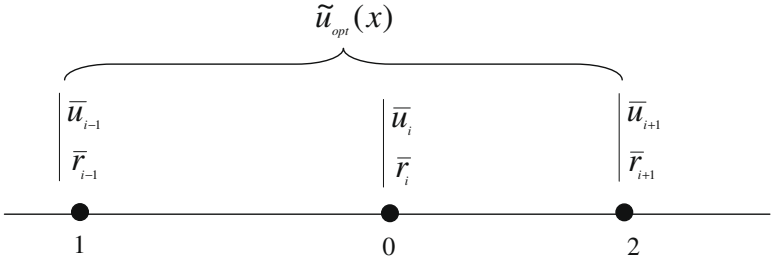

Fig. 2. Three-points stencil for the HLSM reconstruction.

$$\overline{x_i^n} \equiv \frac{1}{\Delta x_i}\int_{I_i}(x-x_i)^n dx \tag{9}$$

We obtain the following result:

$$u_{opt}(x) - \bar{u}_i = \sum_{j=1}^{4} a_j[(x-x_i)^j - \overline{x_i^j}] \tag{10}$$

And, consequently:

$$\frac{1}{\Delta x_j}\int_{I_j}(u_{opt}(x)-\bar{u}_i)dx \equiv \bar{u}_j - \bar{u}_i = a_1\hat{x}_j + a_2\hat{x}_j^2 + a_3\hat{x}_j^3 + a_4\hat{x}_j^4 \quad j \in \{i-1, i+1\} \tag{11}$$

$$\text{where we defined}: \ \hat{x}_j^n \equiv \frac{1}{\Delta x_j}\int_{I_j}[(x-x_i)^n - \overline{x_i^n}]dx \quad j \in \{i-1, i+1\} \tag{12}$$

Therefore, we get the first useful algebraic relation defining the Hermite reconstruction:

$$\bar{u}_j - \bar{u}_i = \sum_{n=1}^{4} a_n \hat{x}_j^n, \quad j \in \{i-1, i+1\} \tag{13}$$

The $\hat{x}_j^n$ terms are metric terms that only depend on the mesh. Using the definition (9), those terms can be developed to give the following results:

$$\begin{cases} \hat{x}_j = (x_j - x_i) \\ \hat{x}_j^2 = (x_j - x_i)^2 + \frac{1}{12}(\Delta x_j^2 - \Delta x_i^2) \\ \hat{x}_j^3 = (x_j - x_i)^3 + \frac{\Delta x_j^2}{4}(x_j - x_i) \\ \hat{x}_j^4 = (x_j - x_i)^4 + \frac{\Delta x_j^2}{2}(x_j - x_i)^2 + \frac{1}{80}(\Delta x_j^4 - \Delta x_i^4) \end{cases} \qquad j \in \{i-1, i+1\} \tag{14}$$

Practically, those terms are pre-calculated and stored in computer memory.

Now, by defining $r_{opt}(x) \equiv \frac{du_{opt}(x)}{dx}$ and by following the same procedure as for $u_{opt}(x)$, we get the second useful algebraic relation:

$$\bar{r}_j - \bar{r}_i = \sum_{n=2}^{4} n a_n \hat{x}_j^{n-1}, \quad j \in \{i-1, i+1\} \tag{15}$$

Then, gathering (13) and (15), we obtain the following algebraic system:

$$\begin{bmatrix} \hat{x}_{i-1} & \hat{x}_{i-1}^2 & \hat{x}_{i-1}^3 & \hat{x}_{i-1}^4 \\ \hat{x}_{i+1} & \hat{x}_{i+1}^2 & \hat{x}_{i+1}^3 & \hat{x}_{i+1}^4 \\ 0 & 2\hat{x}_{i-1} & 3\hat{x}_{i-1}^2 & 4\hat{x}_{i-1}^3 \\ 0 & 2\hat{x}_{i+1} & 3\hat{x}_{i+1}^2 & 4\hat{x}_{i+1}^3 \end{bmatrix} \times \begin{pmatrix} a_1 \\ a_2 \\ a_3 \\ a_4 \end{pmatrix}_i \equiv \begin{bmatrix} L_1 \\ L_2 \\ L_3 \\ L_4 \end{bmatrix} \times \begin{pmatrix} a_1 \\ a_2 \\ a_3 \\ a_4 \end{pmatrix}_i = \begin{pmatrix} \bar{u}_{i-1} - \bar{u}_i \\ \bar{u}_{i+1} - \bar{u}_i \\ \bar{r}_{i-1} - \bar{r}_i \\ \bar{r}_{i+1} - \bar{r}_i \end{pmatrix} \tag{16}$$

At this step, system (16) is a 4×4 system and it generates a fifth-order oscillatory reconstruction.

To introduce monotonicity into the calculation of the derivatives, $\{a_j\}$, let us define over the cell I_i, a low-order monotone polynomial, namely: $u_M(x)$.

This polynomial is defined either by a TVD or by an ENO principle. Then, this polynomial is used in order to produce two supplementary equations:

$$\begin{cases} \frac{1}{\Delta x_{i-1/2}}\int_{x_{i-1}}^{x_i} u_{opt}(x)dx = \frac{1}{\Delta x_{i-1/2}}\int_{x_{i-1}}^{x_i} u_M(x)dx \\ \frac{1}{\Delta x_{i+1/2}}\int_{x_i}^{x_{i+1}} u_{opt}(x)dx = \frac{1}{\Delta x_{i+1/2}}\int_{x_i}^{x_{i+1}} u_M(x)dx \end{cases} \tag{17}$$

In words, the high-order polynomial, $u_{opt}(x)$, must locally coincide, *in average*, with the monotone low-order polynomial, $u_M(x)$. Therefore, using the definition of $u_{opt}(x)$, given by Eq. (10), and then, developing the left-hand side of (17), one obtains two supplementary algebraic conditions for the $\{a_j\}$:

$$\begin{cases} -a_1\frac{\Delta x_{i-1/2}}{2} + a_2\frac{\Delta x_{i-1/2}^2}{4} - a_3\frac{\Delta x_{i-1/2}^3}{4} + 3a_4\frac{\Delta x_{i-1/2}^4}{16} = \frac{1}{\Delta x_{i-1/2}}\int_{x_{i-1}}^{x_i} u_M(x)dx - \bar{u}_i \\ a_1\frac{\Delta x_{i+1/2}}{2} + a_2\frac{\Delta x_{i+1/2}^2}{4} + a_3\frac{\Delta x_{i+1/2}^3}{4} + 3a_4\frac{\Delta x_{i+1/2}^4}{16} = \frac{1}{\Delta x_{i+1/2}}\int_{x_i}^{x_{i+1}} u_M(x)dx - \bar{u}_i \end{cases} \tag{18}$$

Those two relations are re-interpreted as monotonicity constraints to be added to system (16) in order to generate a monotone reconstruction. Consequently, we obtain the following 6×4 over-determined system:

$$\begin{bmatrix} L_1 \\ L_2 \\ L_3 \\ L_4 \\ L_5 \\ L_6 \end{bmatrix} \times \begin{pmatrix} \tilde{a}_1 \\ \tilde{a}_2 \\ \tilde{a}_3 \\ \tilde{a}_4 \end{pmatrix}_i = \begin{pmatrix} \bar{u}_{i-1} - \bar{u}_i \\ \bar{u}_{i+1} - \bar{u}_i \\ \bar{r}_{i-1} - \bar{r}_i \\ \bar{r}_{i+1} - \bar{r}_i \\ B_5 \\ B_6 \end{pmatrix} \Longleftrightarrow L \times A = B \tag{19}$$

$$\text{with}: \begin{cases} L_5 \equiv \left[-\frac{\Delta x_{i-1/2}}{2}, \frac{\Delta x_{i-1/2}^2}{4}, -\frac{\Delta x_{i-1/2}^3}{4}, 3\frac{\Delta x_{i-1/2}^4}{16} \right] \\ L_6 \equiv \left[\frac{\Delta x_{i+1/2}}{2}, \frac{\Delta x_{i+1/2}^2}{4}, \frac{\Delta x_{i+1/2}^3}{4}, 3\frac{\Delta x_{i+1/2}^4}{16} \right] \end{cases} \quad \text{and}: \begin{cases} B_5 \equiv \frac{1}{\Delta x_{i-1/2}} \int_{x_{i-1}}^{x_i} u_M(x)dx - \bar{u}_i \\ B_6 \equiv \frac{1}{\Delta x_{i+1/2}} \int_{x_i}^{x_{i+1}} u_M(x)dx - \bar{u}_i \end{cases} \tag{20}$$

Doing this, it becomes possible to introduce a monotonicity principle into the calculation of the polynomial coefficients, $\{\tilde{a}_j\}$. Using a least-square methodology, i.e. by minimizing the functional $|L \times A - B|^2$, solves this system:

However, the monotonicity principle introduced by (17) is only desirable when the solution is discontinuous or when there exist strong gradients; in regions of smoothness, constraints (17) must be relaxed to obtain the best accuracy for the reconstruction. This process is ensured by the introduction of a data-depending weight, w_i, into (19).

3.2. Weighting of the monotonicity constraints

The principles we adopted to calculate the data-depending weight, w_i, are as follows:

- w_i must smoothly vary between a very small value, in regions of smoothness, and a value $O(1)$ at the location of a discontinuity.
- In regions of smoothness, the modification introduced by w_i must not generate a term that would be greater than the spatial truncature error of the scheme.

To begin, we calculate the general indicator of smoothness over the cell I_i [4]:

$$IS_i \equiv \frac{1}{u_{\max}^2} \sum_k \Delta x_i^{2k-1} \times \int_{I_i} \left(\frac{d^k u_{opt}}{dx^k} \right)^2 dx \tag{21}$$

where $u_{\max}$ is calculated over the whole calculation domain $\Omega : u_{\max} = \max|_{x \in \Omega} u|$. This indicator provides a measure of the smoothness of the solution over the cell I_i, according to the stencil selected to define $u_{opt}(x)$ on that cell. In regions of smoothness, $IS_i << 1$, whereas $IS_i = O(1) > 1$ in cells with strong gradients or discontinuities and tends towards infinity when the mesh is refined. From the definition of $u_{opt}(x)$, formula (21) can be developed to give:

$$IS_i = a_1^2 \Delta x_i^2 + \left(\frac{13}{3} a_2^2 + \frac{1}{2} a_1 a_3 \right) \Delta x_i^4 + \left(\frac{21}{5} a_2 a_4 + \frac{3129}{80} a_3^2 \right) \Delta x_i^6 \tag{22}$$

This formula is valid even on non-uniform meshes. In this formula, the $\{a_j\}$ are solution of system (16). Since this system is a 4×4 system of which the coefficients are only metric terms, *it is inverted once*, at the beginning of the computations, by a direct method; the result is then stored in computer memory. Therefore, it only remains to calculate IS_i, at each time-step, by (22).

Remark. The coefficients $\{a_j\}$ and $\{\tilde{a}_j\}$ should not be confused in formulae above. The coefficients $\{a_j\}$ are solution of (16) and characterize the high-order oscillatory polynomial, $u_{opt}(x)$. The coefficients $\{\tilde{a}_j\}$ are solution of (19) and represent the modified version of $u_{opt}(x)$ to get a monotone reconstruction; henceforth, this polynomial will be noted, $\tilde{u}_{opt}(x)$.

Having calculated the smoothness indicators, IS_i, for each cell I_i, we introduce a normalized smoothness indicator, namely β_i, defined on I_i and such that:

$$\begin{cases} \beta_i \to 0 \text{ in regions of smoothness} \\ \beta_i \to 1^- \text{ if there exist a discontinuity} \end{cases} \text{when } \Delta x \to 0 \tag{23}$$

Practically, we use the formulation experimented in [5]:

$$\beta_i \equiv \frac{(IS_i)^2}{1 + (IS_i)^2}, \quad \forall x \in I_i \tag{24}$$

This normalized smoothness indicator was selected in order to enhance the robustness of the method. Indeed, whatever the problem encountered, this sensor always varies into the interval $[0,1]$; thus, it becomes easier to define a general procedure that adapts automatically to the solution, independently of the magnitude of the discrete variable, $\bar{u}_i$. In addition, this choice

facilitates the calculation of the data-depending weight, w_i, and ensures that this weight introduces a correction that is less than the truncature error when the solution is smooth. This latter point will be checked in a section that follows.

One can demonstrate that $\beta_i = O(\Delta x^4)$ in regions of smoothness of the solution and approaches unity by its lower bound in cells crossed by a discontinuity [5].

Now, we can define the data-depending weight, w_i, that is devised to modulate conditions (18) into the linear system (19):

$$w_i \equiv \alpha \times \beta_i = \frac{\alpha \times IS_i^2}{1 + IS_i^2} \tag{25}$$

where α represents an arbitrary parameter such that $\alpha = O(1)$. In what follows, α will be termed the "monotonicity parameter".

Once w_i is defined, it can be introduced in (19) to weigh the monotonicity constraints (18).

Thus, (19) is modified by the new quantities:

$$\begin{cases} \widetilde{B}_{5,6} \equiv w_i B_{5,6} \to B_{5,6} \\ \widetilde{L}_{5,6} \equiv w_i L_{5,6} \to L_{5,6} \end{cases} \tag{26}$$

All the remaining components of (19) are left unchanged.

Now, to completely define the HLSM reconstruction, it is left to devise the monotone polynomial, namely $u_M(x)$.

3.3. Definition of the monotone polynomial, $u_M(x)$

3.3.1. TVD monotonicity condition

To impose a TVD monotonicity constraint into (19), we select the simplest TVD limiter, known into the literature as the "minmod limiter". Then, on a non-uniform mesh, $u_M(x)$ is simply calculated according to the following formula:

$$u_M(x) \equiv \bar{u}_i + (x - x_i) \times \min\operatorname{mod}\left(\frac{\bar{u}_{i+1} - \bar{u}_i}{\Delta x_{i+1/2}}, \frac{\bar{u}_i - \bar{u}_{i-1}}{\Delta x_{i-1/2}}\right) \quad \forall x \in I_i \tag{27}$$

Thus, it becomes possible to formulate $\widetilde{B}_{5,6}$ in (19):

$$\begin{cases} \widetilde{B}_5 \equiv -w_i \dfrac{\Delta x_i}{2} \times \min\operatorname{mod}\left(\dfrac{\bar{u}_{i+1} - \bar{u}_i}{\Delta x_{i+1/2}}, \dfrac{\bar{u}_i - \bar{u}_{i-1}}{\Delta x_{i-1/2}}\right) \\ \widetilde{B}_6 \equiv w_i \dfrac{\Delta x_i}{2} \times \min\operatorname{mod}\left(\dfrac{\bar{u}_{i+1} - \bar{u}_i}{\Delta x_{i+1/2}}, \dfrac{\bar{u}_i - \bar{u}_{i-1}}{\Delta x_{i-1/2}}\right) \end{cases} \tag{28}$$

The HLSM reconstruction that uses (28) as a monotonicity constraint for (19) will be referenced in what follows as the "HLSM–Minmod" reconstruction.

However, it is well known that the coefficient in the $O(\Delta x)$ term in (17) becomes discontinuous at local extrema, leading to a loss of accuracy at such points. More generally, TVD schemes, independently of their particular form, are necessarily only first-order accurate at local extrema.

To circumvent such a problem, we develop as an alternative a second-order ENO reconstruction. Specifically, this reconstruction is based upon a Hermite formulation of the interpolator: we call this solution, the "HENO2 reconstruction".

3.3.2. ENO monotonicity condition

To devise a HENO2 reconstruction, we use the "reconstruction via a primitive function" technique developed by Harten et al. in [2]. The algorithm that follows is adapted for a Hermite polynomial.

We introduce $H_2(x;\bar{u},\bar{r})$, a piecewise polynomial function of x that interpolates $(\bar{u},\bar{r})$ at the points $\{x_i\}$, i.e.:

$$\begin{cases} \frac{1}{\Delta x_i}\int_{I_i} H_2(x;\bar{u},\bar{r})dx = \bar{u}_i \\ \frac{1}{\Delta x_i}\int_{I_i} \frac{d}{dx} H_2(x;\bar{u},\bar{r})dx = \bar{r}_i \end{cases} \tag{29}$$

$$H_2(x;\bar{u},\bar{r}) \equiv q_{2,j+1/2}(x;\bar{u},\bar{r}) \quad \forall x \in [x_j, x_{j+1}] \tag{30}$$

where $q_{2,j+1/2}$ is a quadratic polynomial in x: it is the unique quadratic polynomial of which the primitive interpolates $(\bar{u}(x),\bar{r}(x))$ over the interval $[x_j, x_{j+1}]$. More precisely, $q_{2,j+1/2}$ can be expressed around the basis point, x_j, to give:

$$q_{2,j+1/2} \equiv D_0 + D_{1,j+1/2} \times (x - x_j) + D_{2,j+1/2} \times (x - x_j)^2 \quad \forall x \in [x_j, x_{j+1}] \tag{31}$$

$$\text{with}: \quad \begin{cases} D_0 = \bar{u}_j - D_{2,j+1/2}\frac{\Delta x_{j+1/2}^2}{12} \\ D_{1,j+1/2} = (\bar{u}_{j+1} - \bar{u}_j - \Delta x_{j+1/2}^2 \times D_{2,j+1/2})/\Delta x_{j+1/2} \end{cases} \tag{32}$$

Therefore, $D_{2,j+1/2}\left(\equiv \frac{1}{2}u_{xx}|_i\right)$ must be determined for the quadratic polynomial, $q_{2,j+1/2}$, to be uniquely determined over the interval $[x_j, x_{j+1}]$.

There are two possibilities to specify $D_{2,j+1/2}$ over $[x_j, x_{j+1}]$.

The first one uses the quantities $\bar{u}_j, \bar{u}_{j+1}, \bar{r}_{j+1}$. In that case, one can specify $D_{2,j+1/2}$, noted $D^+_{2,j+1/2}$:

$$D^+_{2,j+1/2} \equiv \frac{\bar{u}_j - \bar{u}_{j+1} + \Delta x_{j+1/2} \times \bar{r}_{j+1}}{\Delta x^2_{j+1/2}} \tag{33.a}$$

which is such that: $D^+_{2,j+1/2} = \frac{1}{2} u_{xx}|_j + O(\Delta x_j)$.

The second choice for $D_{2,j+1/2}$, noted $D^-_{2,j+1/2}$, relies upon the quantities $\bar{u}_j, \bar{u}_{j+1}, \bar{r}_j$ and gives the following result:

$$D^-_{2,j+1/2} \equiv \frac{\bar{u}_{j+1} - \bar{u}_j - \Delta x_{j+1/2} \times \bar{r}_j}{\Delta x^2_{j+1/2}} \tag{33.b}$$

The polynomial that relies upon the stencil represented by $D^+_{2,j+1/2}$, insists on the numerical information coming from the right of that stencil; using $D^-_{2,j+1/2}$, we insist on the information coming from the left of this same stencil.

Following Harten et al. [2] to uniquely determine $q_{2,j+1/2}$ over $[x_j, x_{j+1}]$, we select the polynomial that is the less oscillatory. This operation is accomplished by defining:

$$D_{2,j+1/2} \equiv \min \mathrm{mod}(D^-_{2,j+1/2}, D^+_{2,j+1/2}) \tag{34}$$

Therefore, we have calculated over $[x_j, x_{j+1}]$ a parabolic polynomial that is such that:

$$\begin{cases} q_{2,j+1/2}(x;\bar{u},\bar{r}) = u(x) + O(\Delta x_j^2) \\ q_{2,j+1/2}(x;\bar{u},\bar{r}) = \bar{u}(x) + O(\Delta x_j^3) \end{cases} \quad \forall x \in [x_j, x_{j+1}] \tag{35}$$

Then, the piecewise function, $H_2(x;\bar{u},\bar{r})$, is defined and can be utilized to construct the monotone polynomial, $u_M(x)$, over the interval I_i. To get en ENO interpolation, we define $u_M(x)$ as follows:

$$u_M(x) = \bar{u}_i + (x - x_i) \times \min \mathrm{mod}\left(\frac{d}{dx} H_2(x_i - 0;\bar{u},\bar{r}), \frac{d}{dx} H_2(x_i + 0;\bar{u},\bar{r})\right) \quad \forall x \in I_i \tag{36}$$

From this choice, it follows that:

(i) wherever $u(x)$ is smooth:

$$\frac{d^k}{dx^k} u_M(x) = \frac{d^k}{dx^k} u(x) + O(\Delta x_i^{3-k}) k \in \{1, 2\} \tag{37.a}$$

(ii) $u_M(x)$ is an essentially non-oscillatory second-order interpolation of u in the sense that:

$$TV(u_M(.)) \leqslant TV(u) + O(\Delta x_i^2) \tag{37.b}$$

Now, we can introduce this polynomial into (18), in order to formulate the ENO-monotonicity constraint for system (19):

$$\begin{cases} \widetilde{B}_5 = -w_i \frac{\Delta x_i}{2} \times \min \mathrm{mod}\left(\frac{d}{dx} H_2(x_i - 0;\bar{u},\bar{r}), \frac{d}{dx} H_2(x_i + 0;\bar{u},\bar{r})\right) \\ \widetilde{B}_6 = w_i \frac{\Delta x_i}{2} \times \min \mathrm{mod}\left(\frac{d}{dx} H_2(x_i - 0;\bar{u},\bar{r}), \frac{d}{dx} H_2(x_i + 0;\bar{u},\bar{r})\right) \end{cases} \tag{38}$$

Therefore, comparing with (28), the HENO formulation introduces an additional term, $D_{2,i\pm1/2} \times \Delta x^2_{i\pm1/2}$, into the calculation of the slope of the solution. This term not only is a function of the variable, u, but also of its first derivative, $r \equiv u_x$, and enables to calculate smooth extrema with a second-order accuracy.

Thus, by using a Hermite interpolation, we have generated a second-order ENO interpolation based on a three-points stencil; this result should be contrasted with the standard ENO2 reconstruction that necessitates a five-points stencil to get an equivalent accuracy.

Combining (19) and (38), the resulting reconstruction will be recognized in what follows as the "HLSM–HENO2" interpolation.

3.4. The HLSM upwind scheme for scalar hyperbolic problems

The final form of the HLSM upwind scheme is given by:

$$\begin{cases} \left.\frac{\partial f}{\partial x}\right|_i = \frac{(\tilde{f}_{i+1/2} - \tilde{f}_{i-1/2})}{\Delta x_i} \\ \left.\frac{\partial g}{\partial x}\right|_i = \frac{(\tilde{g}_{i+1/2} - \tilde{g}_{i-1/2})}{\Delta x_i} \end{cases} \tag{39}$$

and:

$$\begin{cases} u^L_{i+1/2} = \tilde{u}_{opt}(x_{i+1/2}) = \bar{u}_i + \tilde{a}_1 \frac{\Delta x_i}{2} + \tilde{a}_2 \frac{\Delta x_i^2}{6} + \tilde{a}_3 \frac{\Delta x_i^3}{8} + \tilde{a}_4 \frac{\Delta x_i^4}{20} \\ r^L_{i+1/2} = \frac{d}{dx}\tilde{u}_{opt}(x_{i+1/2}) = \bar{r}_i + \tilde{a}_2 \Delta x_i + \tilde{a}_3 \frac{\Delta x_i^2}{2} + \tilde{a}_4 \frac{\Delta x_i^3}{2} \end{cases} \tag{40}$$

$\tilde{f}_{i+1/2}$ and $\tilde{g}_{i+1/2}$ are calculated by the HLLE solver (formulae (5)–(7)). To calculate $\tilde{u}_{opt}(x)$, over I_i, system (19) with modification (26) is inverted. The data-depending weight, w_i, is calculated according to (25) and the monotone polynomial, $u_M(x)$, that defines $\widetilde{B}_{5,6}$ is calculated by selecting either a TVD-monotonicity constraint (formula (28)) or an ENO-monotonicity constraint (formula (38)).

The result is a polynomial, $\tilde{u}_{opt}(x)$, locally defined over the cell I_i, and conceived to be non-oscillatory, *in the mean* (conditions (17)). The resulting scheme is spatially fifth-order accurate in smooth regions of the solution and tends towards a first-order accuracy in regions crossed by a discontinuity.

Remark. Practically, system (19) is inverted by using Householder transforms to reduce the left-hand side of (19) to upper-triangular form. When the cell aspect ratio gets very large, one can note some conditioning problems if one use normal equations to solve the least-square problem. Householder transforms are much less sensitive to the matrix condition number [6]; this implies a greater robustness of the resulting method.

3.5. Extension to non-linear systems: the one-dimensional Euler equations

In this section, we extend the HLSM scheme to solve systems of hyperbolic conservation laws. Specifically, we consider the one-dimensional Euler equations in the following conservation form:

$$\frac{\partial \mathbf{U}}{\partial t} + \frac{\partial \mathbf{F}(U)}{\partial x} = 0 \tag{41}$$

$$\text{where :} \quad \mathbf{U} \equiv [\rho, \rho u, \rho E]^t, \quad \mathbf{F} \equiv [\rho u, \rho u^2 + p, \rho u H]^t \tag{42}$$

$H \equiv E + p/\rho$ is the specific total enthalpy and this set of equations is closed by the equation-of- state of an ideal gas: $p = (\gamma - 1)(\rho E - u^2/2), \gamma = 1.40$.

In order to use a Hermite procedure, we derive the following set of systems from (41):

$$\begin{cases} \frac{\partial \mathbf{U}}{\partial t} + \frac{\partial \mathbf{F}(U)}{\partial x} = 0 \\ \frac{\partial \mathbf{V}}{\partial t} + \frac{\partial \mathbf{G}(U,V)}{\partial x} = 0 \end{cases} \tag{43}$$

where we defined: $\mathbf{V} \equiv [(\rho)_x, (\rho u)_x, (\rho E)_x]^t, \mathbf{G} \equiv [(\rho u)_x, (\rho u^2 + p)_x, (\rho u H)_x]^t$.

As in the scalar case, the semi-discrete conservative finite-volume scheme discretizing (43) is then written as:

$$\begin{cases} \frac{d\bar{\mathbf{U}}_i}{dt} = -\frac{1}{\Delta x_i}[\widetilde{\mathbf{F}}_{i+1/2} - \widetilde{\mathbf{F}}_{i-1/2}] \\ \frac{d\bar{\mathbf{V}}_i}{dt} = -\frac{1}{\Delta x_i}[\widetilde{\mathbf{G}}_{i+1/2} - \widetilde{\mathbf{G}}_{i-1/2}] \end{cases} \tag{44}$$

To calculate $(\widetilde{F}_{i+1/2}, \widetilde{\mathbf{G}}_{i+1/2})$, the HLLE solver defined in the scalar case by (5)–(7), is simply extended to the case of the Euler equations by re-defining the characteristic velocities $\lambda^{\pm}_{i+1/2}$:

$$\begin{cases} \lambda^+_{i+1/2} \equiv \max(u^L_{i+1/2} + a^L_{i+1/2}, u^R_{i+1/2} + a^R_{i+1/2}, \bar{u}_{i+1/2} + \bar{a}_{i+1/2}, 0) \\ \lambda^-_{i+1/2} \equiv \min(u^L_{i+1/2} - a^L_{i+1/2}, u^R_{i+1/2} - a^R_{i+1/2}, \bar{u}_{i+1/2} - \bar{a}_{i+1/2}, 0) \end{cases} \tag{45}$$

where $a^{L,R}_{i+1/2} \equiv \sqrt{\frac{\gamma p}{\rho}}\Big|^{L,R}_{i+1/2}$ is the speed of sound for an ideal gas and $(\bar{u}_{i+1/2}, \bar{a}_{i+1/2})$ are calculated by using Roe's average.

The conservative point-values, $\left(\mathbf{U}^{L,R}_{i+1/2}, \mathbf{V}^{L,R}_{i+1/2}\right)$, are calculated from the interpolated primitive variables $\left[\rho^{L,R}_{i+1/2}, u^{L,R}_{i+1/2}, p^{L,R}_{i+1/2}\right]^t$ and $\left[(\rho_x)^{L,R}_{i+1/2}, (u_x)^{L,R}_{i+1/2}, (p_x)^{L,R}_{i+1/2}\right]^t$. Those variables are interpolated by using the HLSM procedure developed in the scalar case. We ensure the time-integration of (44) by using the third-order TVD Runge–Kutta procedure [12].

4. Numerical validation

4.1. Spectral analysis

Our purpose is twofold: firstly to study the linear stability of the method, secondly to estimate the influence of the monotonicity parameter, α.

Technical details concerning this sub-section are given in Appendix. To simplify the notations, we suppose that the mesh is uniform ($\Delta x_i = \Delta x \equiv Cte$).

To study the spectral behaviour of the HLSM scheme, we consider the linear system that follows:

$$U_t + aU_x = 0 \quad (a \equiv Cte > 0) \tag{46}$$

with: $U \equiv [u, r \equiv u_x]^t$.

Using the so-called "method of lines" and first discretizing the spatial operator, produce the following system of ODEs in time:

$$\left.\frac{dU}{dt}\right|_i + a\frac{U^L_{i+1/2} - U^L_{i-1/2}}{\Delta x} = 0 \tag{47}$$

Then, a discrete Fourier transform gives the following result (see Appendix for a detailed explanation):

$$\frac{d\widehat{U}}{dt} = G(\beta, \nu, \alpha) \times \widehat{U} \tag{48}$$

Finally, integrating this result by the third-order TVD Runge–Kutta scheme [12] over the interval $[t_n, t_{n+1}]$, we get:

$$\widehat{U}^{n+1} = \mathcal{G}(\beta, \nu, \alpha) \times \widehat{U}^n \tag{49}$$

In the Fourier space, this relation is equivalent to the integrated form of (47) in the physical space. Therefore, to study the structure of the 2×2 complex matrix, Γ, is equivalent to analyze the space-time properties of the algebraic form discretizing (46).

This complex matrix, $\Gamma(\beta, \nu, \alpha)$, – also called in the literature, the "complex amplification matrix" – makes it possible to define the following quantities (see Appendix for details):

- the "accurate" and "spurious" eigenvalues;
- discretization and "spurious" errors;
- the truncature error;
- the amplitude and phase errors.

All these quantities can be expressed in terms of the three parameters of this study: the number of cells-per-wavelength, $N(N \times \beta = 2\pi)$, the CFL number, ν $(\equiv a\Delta t/\Delta x)$ and the monotonicity parameter, α, introduced to modulate w_i, (formula (25)).

To begin this analysis, we select the case $w_i = \alpha \times \Delta x^4$ into the algebraic relations defining the HLSM interpolation. In other words, we suppose that the numerical solution lies in a region of smoothness: in such a case, the choice of the monotonicity constraint is indifferent.

Unless mentioned, the CFL number is set to 0.8 in those results. Fig. 3 presents results for a centred initialization of the first-derivative $(r(x_i, t = 0) = (u(x_{i+1}, t = 0) - u(x_{i-1}, t = 0))/2\Delta x)$.

As one can note it, the modulus of both accurate and spurious eigenvalues remains everywhere below unity: the scheme is linearly stable, Fig. 3(a). This is true as long as the CFL is lower than the unity; in the opposite case, the modulus of the accurate eigenvalue becomes greater than one and the scheme is unstable. Fig. 3(b) shows a very interesting result: at a given time $(t = 100 \times \Delta t)$ and whatever the spatial discretization selected (β varying), the "spurious" error remains lower than the truncature and the discretization errors. To verify if this result is preserved in time, we present Fig. 3(c): as we can note it, the magnitude of the "spurious" error on a given mesh – $N = 10$ cells-per-wavelength: a reasonable choice for a high-order scheme – decreases very rapidly when the time grows up. Therefore, we can conclude that the spurious component of the numerical solution never "pollutes" the accurate component of that solution. Finally, Fig. 3(d), checks the global accuracy of the method by plotting the truncature error versus the phase angle: the global third-order accuracy is confirmed.

Furthermore, we can analytically formulate in the Fourier space, the spatial truncature error, $\hat{\tau}(\beta)$, when $\beta \to 0$ (see Appendix). Indeed, by using a Taylor series expansion, the result is the following:

$$\hat{\tau} = \frac{1}{360}\beta^5 + O(\beta^6) \tag{50}$$

Obviously, this result indicates that the spatial accuracy of the scheme – fifth-order accuracy –, is free of the value of the monotonicity parameter, α. Therefore, we can conclude that *α has no influence on the accuracy of the solution in regions of smoothness*: α is only selected to optimize the capture of discontinuities.

Now, if we modify the initialization process of the first-derivative, the result is somewhat different: this is illustrated by Fig. 4. For an upwind first-order discretization, the level of the initial error becomes higher: in some cases $(N \geqslant 35)$ this increase can generate a "spurious" error greater than the truncature error, Fig. 4(a). However, even in this case, the "spurious" error rapidly decreases when the time grows up, Fig. 4(b). This tendency is unchanged when the first derivative is initialized to the zero value, Fig. 4(c) and (d).

Lastly, Fig. 5 presents the levels of the amplitude and phase errors according to N and the CFL.

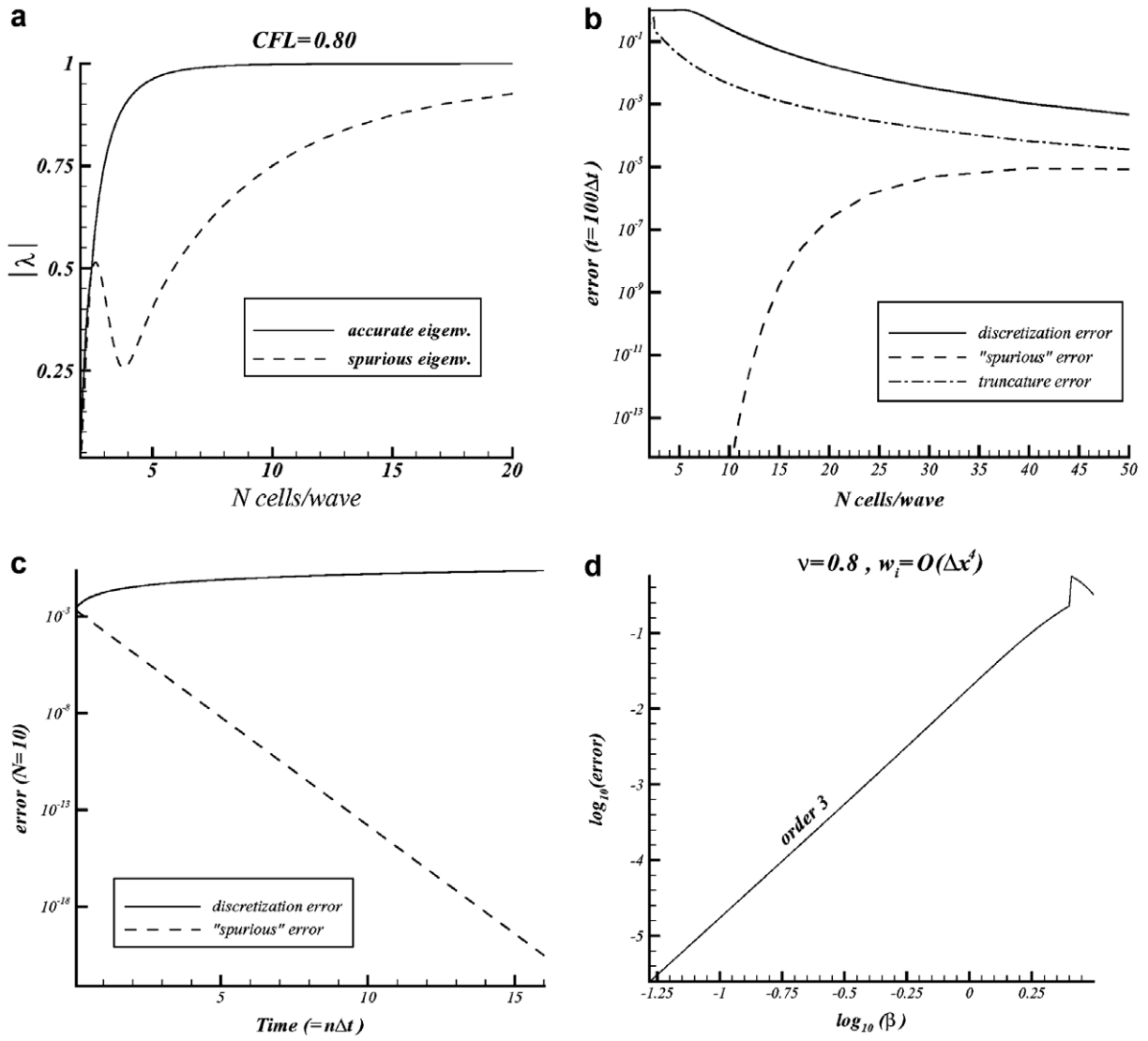

Fig. 3. Spectral analysis for the HLSM scheme (centred initialization of the derivative): $\nu = 0.80$, $w_i = \alpha \times \Delta x^4$. (a) Accurate and spurious eigenvalues; (b) spatial evolution of errors at $t_n = 100 \times \Delta t$; (c) temporal evolution of errors for $N = 10$ cells-per-wavelength; (d) total truncature error.

As one can see it, only 12 cells-per-wavelength are necessary to get an amplitude error at 0.1% for CFL = 0.8. For this latter value, less than 10 cells-per-wavelength are necessary to get a 0.1% phase error.

Now, we look at the case $w_i = O(\alpha)$.

As already mentioned, this case can correspond to two cases: (i) the presence of a discontinuity into the solution, (ii) the existence of an extremum. Let us study the first case.

When a discontinuity exists, both monotonicity constraints (TVD and ENO) return the zero value for the local slope of the solution ($\widetilde{B}_5 = \widetilde{B}_6 = 0$). Inserting this result into the complex amplification matrix, we obtain the following result concerning the spatial truncature error:

$$\hat{\tau} = \frac{\alpha^2}{2(\alpha^2+4)}\beta + O(\beta^2) \tag{51}$$

As predicted, the scheme becomes first-order; moreover, the size of the truncature error now depends on the value of α: the dissipative nature of the scheme can be modulated by the value of α. This result means that the numerical handling of a discontinuity will be influenced by the choice of the parameter, α. Fig. 6(a) and (b) present numerical phase and amplitude errors for this case: comparing to Fig. 5 the loss of accuracy is clearly visible.

Now, let us have a look to the second case, i.e. the existence of a smooth extremum into the solution while $w_i = O(\alpha)$. Obviously, there is no change if the monotonicity condition relies upon a TVD principle since it returns the zero value for

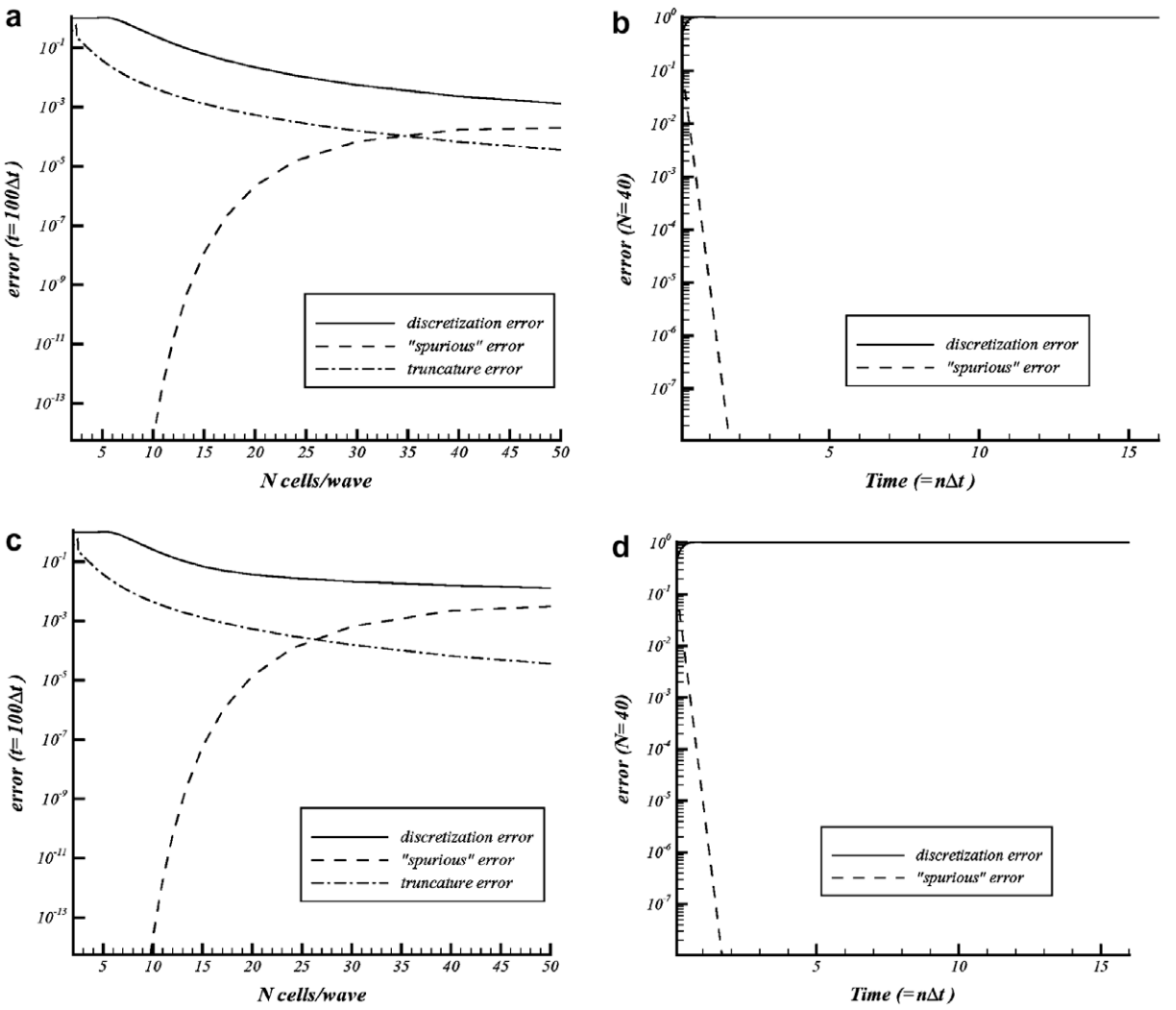

Fig. 4. Spectral analysis for the HLSM scheme: $v = 0.80$, $w_i = \alpha \times \Delta x^4$. Initialization of the first derivative: (a, b) $r(x_i, t = 0) = \frac{u(x_i,t=0)-u(x_{i-1},t=0)}{\Delta x}$; (c, d) $r(x_i, t = 0) \equiv 0$. (a, c) Spatial evolution of errors at $t_n = 100 \times \Delta t$; (b, d) temporal evolution of errors for $N = 40$ cells-per-wavelength.

the slope of the solution. Therefore, suppose we select the ENO condition (38) to define the HLSM scheme. In this case, we obtain the following result for the spatial truncature error:

$$\hat{\tau} = \frac{77\alpha^2}{15(49\alpha^2 + 256)}\beta^2 + O(\beta^3) \tag{52}$$

Thus, the ENO-monotonicity constraint generates a second-order scheme in that case. Clearly, this is an improvement when compared with a TVD constraint. This result is illustrated by Fig. 6(c) and (d): for a given CFL number and a fixed spatial resolution (N), the error level is lower than the one presented by Fig. 6(a) and (b).

Summarizing, this analysis gives us two significant results:

- The accuracy of the scheme is free of the monotonicity parameter, α. This parameter is only useful to optimize the capture of possible discontinuities.
- The initialization process of the first-derivative has no influences upon the stability or the accuracy of the scheme as long as the CFL is lower than one.

Incidentally, this analysis shows us the benefit we can hope by employing an ENO-monotonicity constraint when there are smooth data for which $w_i = O(1)$.

For the entire scalar test-cases that follow, the monotonicity parameter, α, is set to the value 6. This value was optimized by trial and errors when discontinuities are present into the solution.

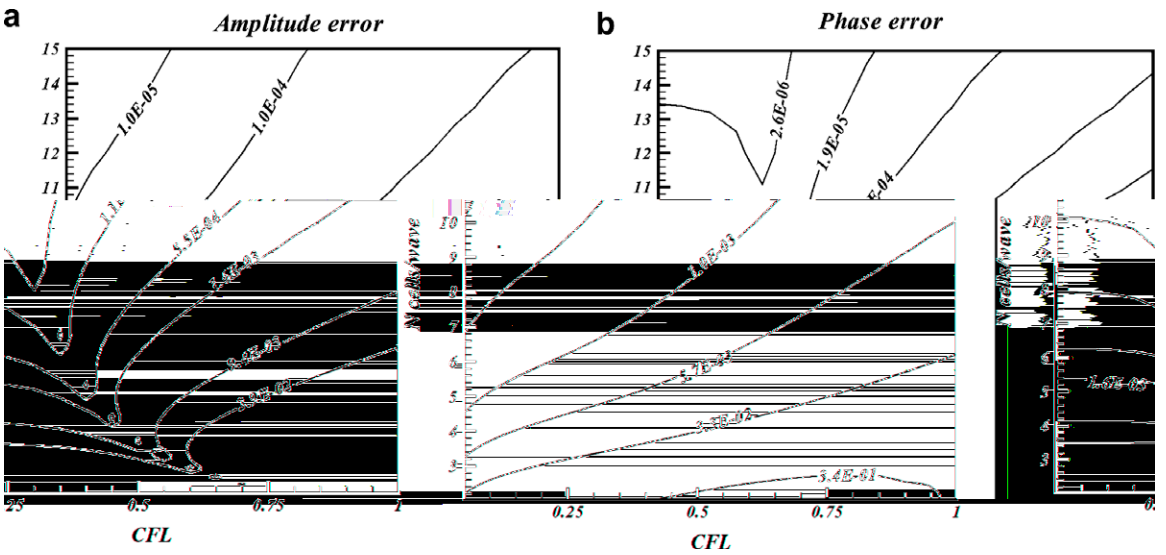

Fig. 5. Spectral analysis for the HLSM scheme: $v = 0.80,\ w_i = \alpha \times \Delta x^4$. (a) Amplitude error; (b) phase error.

4.2. Non-linear scalar problem: the Burgers equation

We solve the following non-linear scalar Burgers equation:

$$u_t + \left(\frac{u^2}{2}\right)_x = 0 \quad \forall x \in [0,2] \tag{53}$$

with the initial condition: $u(x, t = 0) = 1/2 + \sin(\pi x)$ and a 2-periodic boundary condition. To begin, a uniform mesh with N cells is used for this test case. For those results, we utilize the HUWENO5 scheme of Qiu and Shu as a Ref. [11]. The CFL number is defined as: $\max_i |u_i^n| \Delta t / \min_i \Delta x_i$. Unless mentioned, its value is taken as 0.5 for both HLSM and HUWENO5 schemes. For the accuracy tests, since the time integration method incurs $O(\Delta t^3)$ errors, the time step is chosen to be $\Delta t = O(\Delta x^2)$ in order for the discretization error of the overall scheme to be a measure of the spatial convergence only.

When $t = 1/2\pi$, the solution is still smooth and the discrete errors (L_1 and L_∞ norms) and numerical orders of accuracy are shown in Table 1 (HLSM–Minmod scheme), Table 2 (HLSM–HENO2 scheme) and Table 3 (HUWENO5 scheme). As can be seen, all the schemes reach their designed order of accuracy; however, the HLSM–HENO2 version produces the best results on coarse meshes. This latter result indicates that the monotonicity constraint is active on coarse meshes: this means that the data-depending weight, w_i, is not always negligible on such meshes. However, when $N > 40$, both versions of the HLSM scheme produce equivalent results; those results remain better than those obtained with the HUWENO5 scheme.

When $t = 3/2\pi$, a shock has already appeared in the solution and it is located at $x = 1.238$.

Fig. 7 shows the numerical solution for both versions of the HLSM scheme on a uniform mesh with $N = 80$ grid points. As one can note it, the shock is captured without any numerical oscillation in all cases, Fig. 7(a) and (b). Moreover, there are no obvious differences between the Minmod and the ENO version of the scheme, Fig. 7(b) and (c). This is true either for the solution itself, Fig. 7(b), or for the discretization error, Fig. 7(c). Lastly, Fig. 7(d) shows the evolution of $w_i$in the computation domain: only four values are $O(1)$. It is at these points that the monotonicity constraints play a role.

Fig. 8(a) shows the numerical solution on a stretched mesh ($\Delta x_{\min}/\Delta x_{\max} = 0.10$) near the shock place: the shock is captured without any numerical oscillations. In Fig. 8(b), we compare the HLSM–HENO2 scheme with the HUWENO5 scheme: in both cases, the shock is captured in the same way though those schemes are structurally very different.

Consequently, the monotonicity constraints, (17), produce numerical results that are equivalent to those obtained via a more "classical" WENO procedure. In addition, the HLSM scheme is more accurate on smooth data.

4.3. Nonconvex flux

We use a nonconvex flux to test the convergence of the scheme to the physically correct solution. The "exact" solutions are obtained from the HLSM scheme on a very fine grid. All the results presented below are obtained with N = 80 grid points. The flux is selected as:

$$f(u) = \frac{1}{4}(u^2 - 1)(u^2 - 4) \quad \text{with the initial data}: u(x, t = 0) = \begin{cases} 2 & x < 0 \\ -2 & x > 0 \end{cases} \tag{54}$$

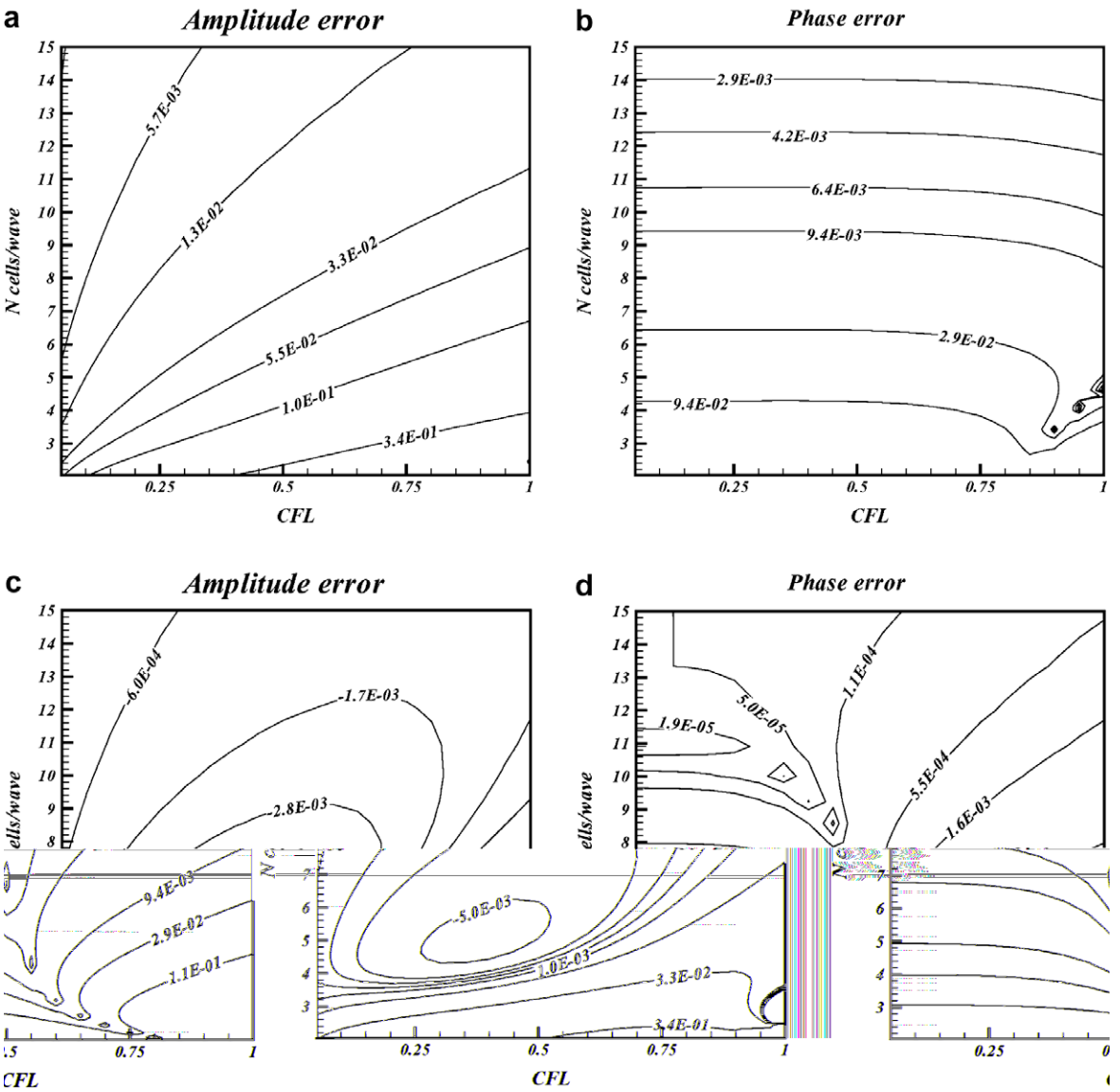

Fig. 6. Spectral analysis for the HLSM scheme. Discontinuous case: $w_i = O(1)$. (a, b) HLSM–Minmod; (c, d) HLSM–HENO2.

Table 1
$u_t + uu_x = 0; u(x, t = 0) = 1/2 + \sin(\pi \times x)$; HLSM–Minmod scheme ($\alpha = 6$) with periodic boundary conditions; $t = 1/2\pi$; $\Delta t = \Delta x^2/2$; L_1 and L_∞ errors.

N	L_1 Error	L_1 Order	L_∞ Error	L_∞ Order
10	1.36×10^{-2}	–	2.56×10^{-2}	–
20	5.01×10^{-4}	4.8	2.32×10^{-3}	3.1
40	8.05×10^{-6}	5.9	4.18×10^{-5}	5.8
80	2.52×10^{-7}	5	1.95×10^{-6}	5
160	8.27×10^{-9}	5	6.35×10^{-8}	5

The exact solution is a centred rarefaction wave between two discontinuities, Fig. 9. Numerical results are presented at $t = 1.20$. Both versions of the HLSM scheme converge to entropy correct solution and there are not visible differences between those versions.

Table 2
$u_t + uu_x = 0; u(x, t = 0) = 1/2 + \sin(\pi \times x)$; HLSM–HENO2 scheme ($\alpha = 6$) with periodic boundary conditions; $t = 1/2\pi;\ \Delta t = \Delta x^2/2;\ L_1$ and L_∞ errors.

N	L_1 Error	L_1 Order	L_∞ Error	L_∞ Order
10	4.78×10^{-3}	–	6.90×10^{-3}	–
20	1.75×10^{-4}	4.7	7.69×10^{-4}	3.1
40	7.96×10^{-6}	4.8	4.18×10^{-5}	4.2
80	2.52×10^{-7}	4.9	1.95×10^{-6}	5
160	8.27×10^{-9}	5	6.35×10^{-8}	5

Table 3
$u_t + uu_x = 0; u(x, t = 0) = 1/2 + \sin(\pi \times x)$; HUWENO5 scheme with periodic boundary conditions; $t = 1/2\pi;\ \Delta t = \Delta x^2/2;\ L_1$ and L_∞ errors.

N	L_1 Error	L_1 Order	L_∞ Error	L_∞ Order
10	3.66×10^{-3}	–	7.29×10^{-3}	–
20	1.86×10^{-4}	4.1	8.03×10^{-4}	3
40	1.07×10^{-5}	3.9	6.06×10^{-5}	3.5
80	3.54×10^{-7}	4.9	2.73×10^{-6}	4.5
160	1.20×10^{-8}	4.9	9.27×10^{-8}	4.9

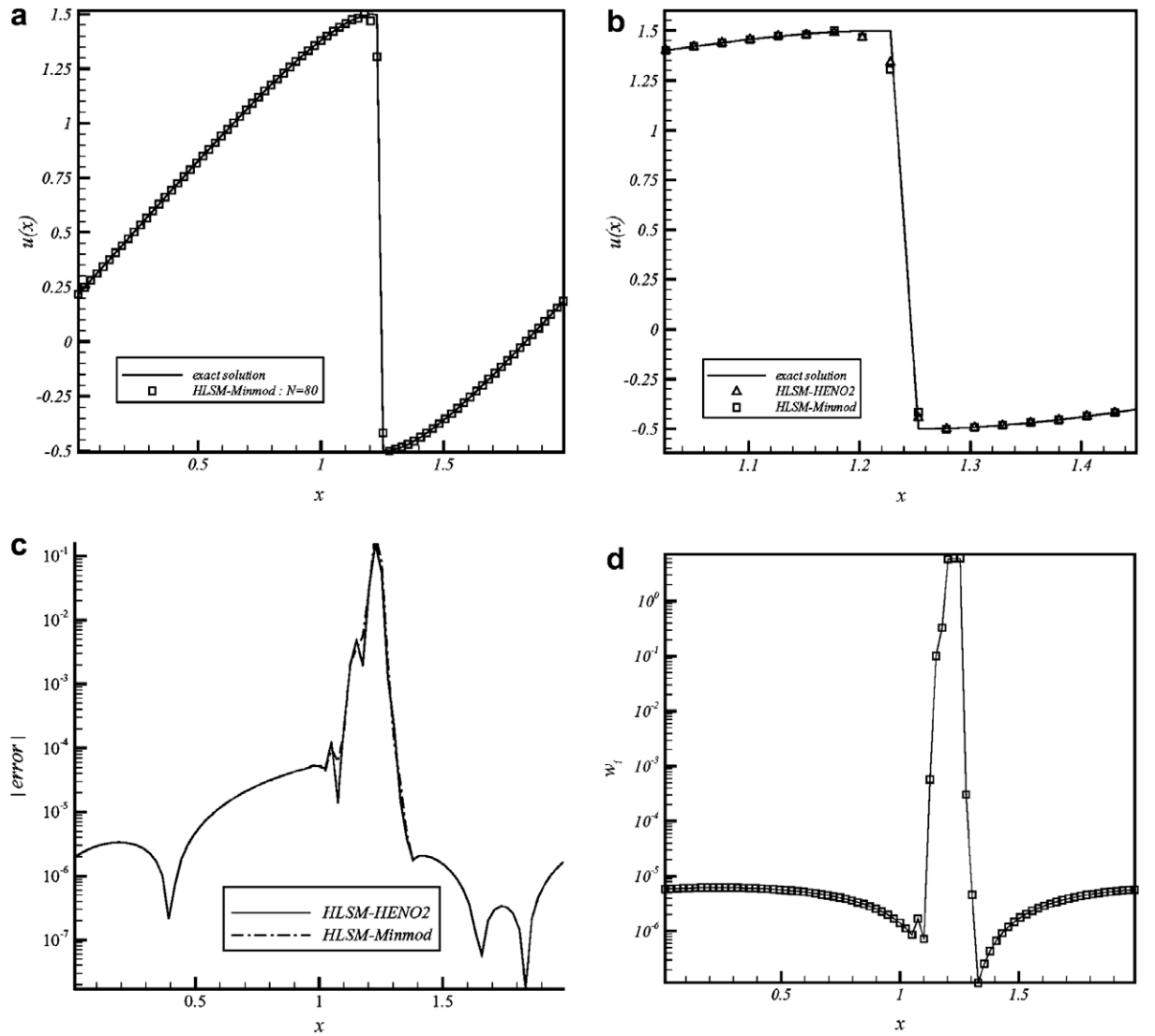

Fig. 7. Burgers equation. $u(x, t = 0) = 1/2 + \sin(\pi x),\ t = 3/2\pi,\ N = 80,\ \mathrm{CFL} = 0.5,\ \alpha = 6$. HLSM scheme: (a) HLSM–Minmod, (b) Comparison Minmod/HENO2, (c) discretization error, (d) data-depending weight, w_i.

4.4. One-dimensional hyperbolic systems: the Euler equations

In what follows and unless mentioned, *all the test cases are run with the value 2 for the monotonicity parameter*, α. This value is selected as the best compromise for the cases investigated and demonstrates the robustness of the method presented. However, we shall show on some cases that the numerical results can be substantially improved if we modify α.

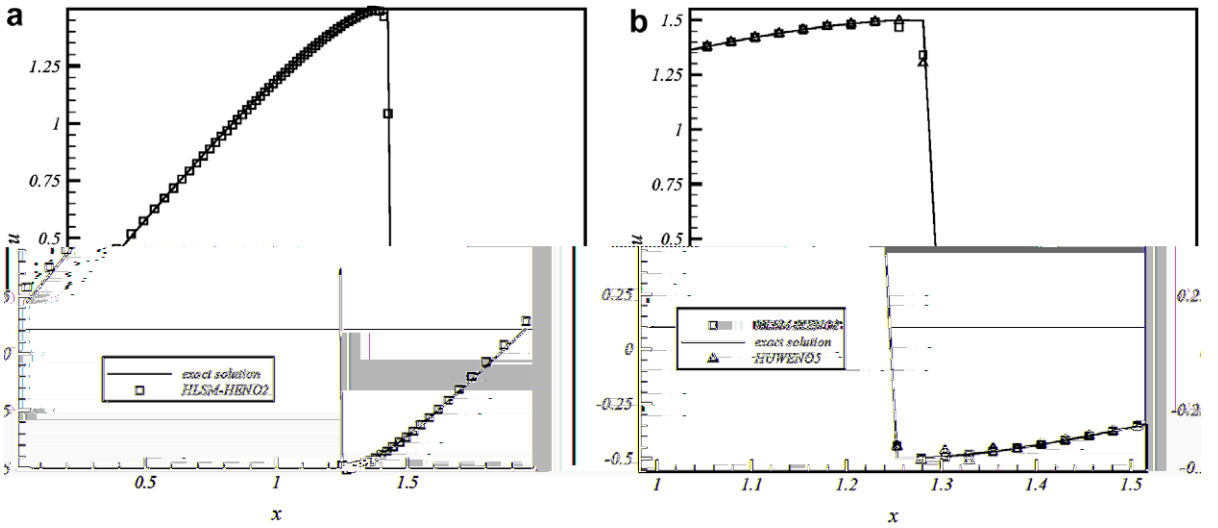

Fig. 8. Burgers equation. $u(x,t=0)=1/2+\sin(\pi x),\ t=3/2\pi,\ N=80,\ \mathrm{CFL}=0.5,\ \alpha=6$. (a) HLSM–HENO2: non-uniform mesh ($\Delta x_{\min}/\Delta x_{\max}=0.1$). (b) Comparison between the HLSM–HENO2 scheme and the HUWENO5 scheme.

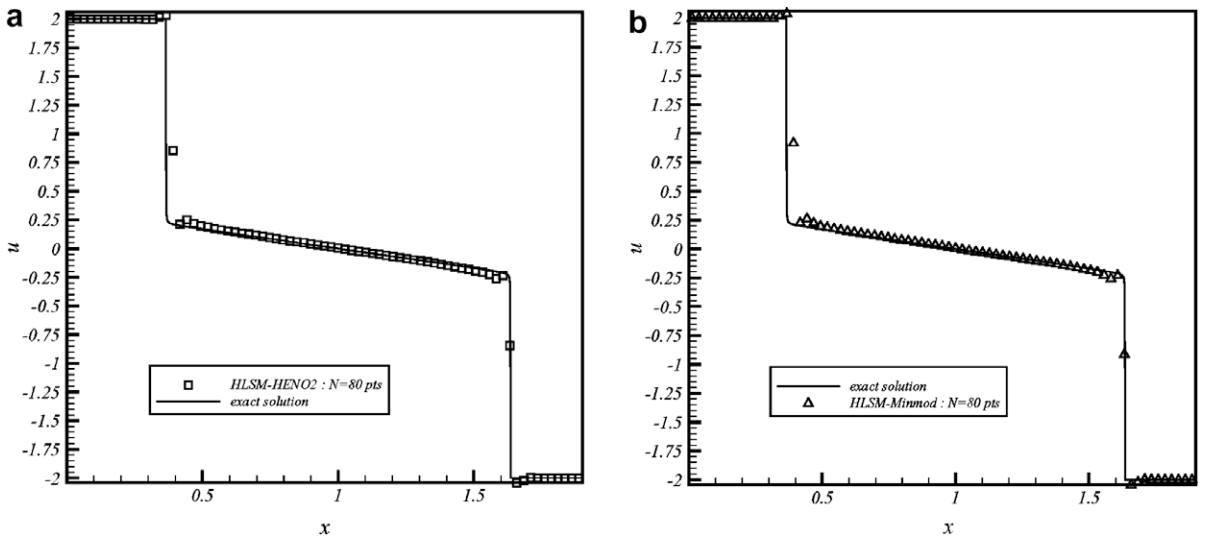

Fig. 9. Nonconvex flux: $f(u)=\frac{1}{4}(u^2-1)(u^2-4),\ u_l=2,\ u_r=-2.\ t=1.20,\ N=80,\ \mathrm{CFL}=0.5,\ \alpha=6$. (a) HLSM–HENO2, (b) HLSM–Minmod.

Table 4
One-dimensional Euler equations $\rho(x,t=0)=1+0.2\times\sin(\pi x),\ u(x,t=0)=1,\ p(x,t=0)=1$ HLSM–Minmod/HENO2 ($\alpha=2$) scheme with periodic boundary conditions $t=2;\ \Delta t=\Delta x^2/2;\ L_1$ and L_∞ errors of density ρ.

N	L_1 Error	L_1 Order	L_∞ Error	L_∞ Order
10	4.42×10^{-3}	–	3.45×10^{-3}	–
20	1.04×10^{-4}	5.4	8.13×10^{-5}	5.3
40	2.70×10^{-6}	5.2	2.12×10^{-6}	5.2
80	7.55×10^{-8}	5.2	5.93×10^{-8}	5.1
160	2.23×10^{-9}	5.1	1.88×10^{-9}	5

The computations are run on a uniform mesh ($\Delta x_i \equiv Cte$), except for the last test-case. N grid points are utilized to discretize the equations.

The CFL number is defined as:

$$\mathrm{CFL} \equiv \Delta t \times \frac{\max_i(|u_i| + a_i)}{\Delta x}$$

We choose CFL = 0.80 for almost all test cases, except for the accuracy tests.

Example 1. We solve the Euler equations, (41), in the domain [0,2]. The initial condition is set to be: $\rho(x, t = 0) = 1 + 0.2 \times \sin(\pi x),\ u(x, t = 0) = 1,\ p(x, t = 0) = 1$, with a 2-periodic boundary condition. The numerical solution is computed up to $t = 2$ with $\Delta t = O(\Delta x^2)$ (HLSM and HUWENO5 schemes). The errors and numerical orders of accuracy of the density, ρ, for the HLSM–HENO2 scheme (resp. HUWENO5 scheme) are shown in Table 4 (resp. Table 5). Results obtained with the Minmod version are identical to the HENO2 version, even on coarse meshes. Both schemes reach their theoretical order of accuracy and the HLSM and HUWENO5 schemes give equivalent results for this problem.

Example 2 (*Lax problem).* The Lax problem is defined by the following left- and right-initial states:

$$(\rho, u, p) = (0.445, 0.698, 3.528) \quad \forall x \leqslant 0, \qquad (\rho, u, p) = (0.5, 0, 0.571) \quad \forall x > 0$$

N = 100 grid points are used to discretize the computational domain [0,1]. The solution is run up to $t = 1.30$. Numerical results are presented for the HLSM–HENO2 (Fig. 10-left) and the HLSM–Minmod schemes (Fig. 10-right). Differences between both versions are clearly visible for this test case: the density profile is less oscillatory with the HENO2 version (Fig. 10-left), while the pressure profile is better calculated by the HLSM–Minmod version (Fig. 10-right).

The contact discontinuity is smeared more than the shock but oscillations are clearly visible close to the contact discontinuity, Fig. 10. The oscillatory behaviour of the component-wise reconstruction is even more pronounced in the velocity profile. It should however be pointed out that, on the same mesh, these oscillations are less "noisy" than more classical component-wise reconstructions such as the ENO scheme [2] or the CWENO scheme [17]. Moreover, those oscillations become less significant when the mesh is refined.

Those results can be compared with the HUWENO5 scheme, Fig. 11-left: the HUWENO5 scheme gives results that are less oscillatory when compared with the HLSM scheme. However, one must note that the contact discontinuity and the shock-wave are more attenuated by the HUWENO scheme: clearly, this scheme is more dissipative. This dissipative nature, which is an advantage in such a case, will become a drawback in tests that follow.

To improve those results, we could increase the dissipative nature of the HLSM scheme by increasing the monotonicity parameter, α, in (25). For example, Fig. 11-right presents results obtained by the HLSM–Minmod procedure with $\alpha = 15$: comparing to Fig. 10, oscillations are significantly reduced; however, the contact discontinuity and the shock are more dissipated, now.

Consequently, keeping the same value for the monotonicity parameter α, the HLSM scheme has the important advantage to tolerate component-wise reconstructions, without generating too many significant non-physical oscillations. Those oscillations decay with the mesh, confirming the monotonicity behaviour of the scheme.

Example 3 (*Shock interaction with entropy waves: the Shu–Osher problem [12]).* We solve the Euler equations, (41), with a moving Mach = 3 shock interacting with sine waves in density. The initial condition is defined as:\

$$(\rho, u, p) = (3.857143, 2.629369, 10.333333) \quad \forall x < -4$$
$$(\rho, u, p) = (1 + \delta \sin 5x, 0, 1) \quad \forall x \geqslant -4$$

For this test, we take $\delta = 10^{-2}$. The computed density ρ is plotted at $t = 1.8$ against the "exact" solution; this solution is a converged solution computed by the HLSM scheme with 2500 grid points.

For $N = 200$ grid points, we compare the numerical results obtained with the HLSM–HENO2, Fig. 12(a), and the HLSM–Minmod schemes, Fig. 12(b): results are identical and the complex wave patterns after the shock entropy wave interaction are well predicted; moreover, we can note that as long as α varies around an $O(1)$ value, the smooth part of the solution

Table 5
One-dimensional Euler equations $\rho(x, t = 0) = 1 + 0.2 \times \sin(\pi x),\ u(x, t = 0) = 1,\ p(x, t = 0) = 1$ HUWENO5 scheme with periodic boundary conditions $t = 2;\ \Delta t = \Delta x^2/2;\ L_1$ and L_∞ errors of density ρ.

N	L_1 Error	L_1 Order	L_∞ Error	L_∞ Order
10	5.44×10^{-3}	–	4.25×10^{-3}	–
20	1.33×10^{-4}	5	1.04×10^{-4}	5
40	3.64×10^{-6}	4.9	2.86×10^{-6}	4.9
80	1.06×10^{-7}	5.1	8.36×10^{-8}	5.1
160	3.22×10^{-9}	4.9	2.66×10^{-9}	4.8

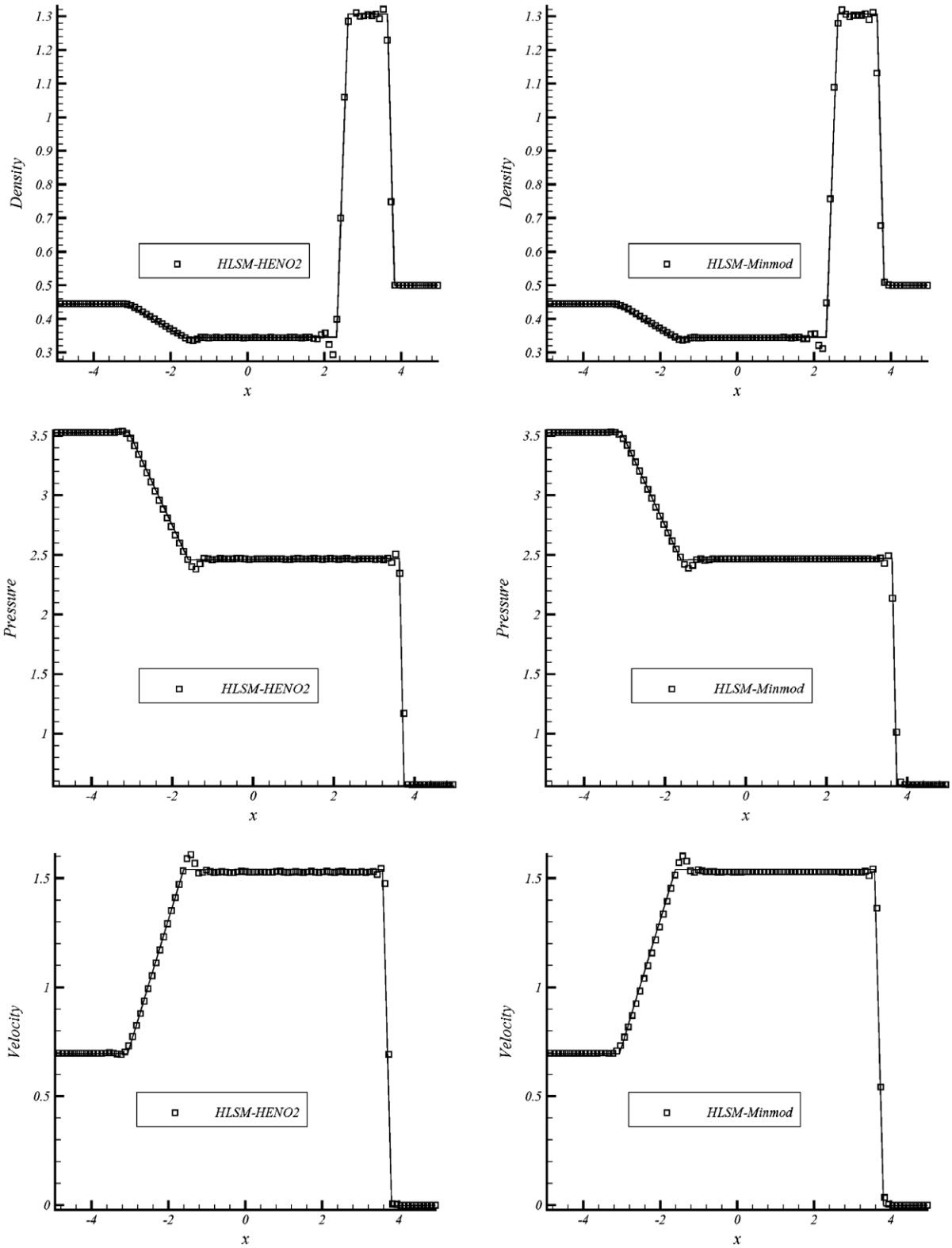

Fig. 10. The Lax problem. HLSM scheme. ($N = 100,\ t = 1.30,\ \mathrm{CFL} = 0.5,\ \alpha = 2$). Left: HLSM–HENO2, Right: HLSM–Minmod.

remains unaltered. Comparing those results to those of the HUWENO5 scheme, Fig. 12(c), we can appreciate the dissipative nature of the HUWENO5 scheme since $N = 300$ grid points are necessary to get an equivalent accuracy.

Example 4 (*Shock entropy wave interactions [4]*). This problem is very suitable for high-order shock-capturing schemes because both shocks and complicate smooth flow features co-exist. In this example, a moving shock interacts with an entropy wave of small amplitude.

On the domain [0,5], the initial condition is the following:

$$(\rho, u, p) = (3.857143, 2.629369, 10.333333) \quad \forall x < 1/2$$
$$(\rho, u, p) = (e^{-\varepsilon \sin(kx)}, 0, 1) \quad \forall x \geqslant 1/2$$

where ε and k are the amplitude and the wave number of the entropy wave, respectively.

The mean flow is a right moving Mach 3 shock. If ε is small compared to the shock strength, the shock will go to the right of the computational domain, at approximately the non-perturbed shock speed and generate a sound wave that travels along with the flow behind the shock. At the same time, the small amplitude, low-frequency entropy waves are generated in front of the shock. After having interacted with the shock, these waves are compressed in frequency and amplified in amplitude.

The main goal of such a test is to check if the structure of the amplified waves is not lost after having crossed the shock wave. Since the entropy wave is very weak relative to the shock, any excessive numerical oscillation could alter the generated waves and the entropy waves.

In our computations, we take $\varepsilon = 0.01$. Accordingly, the amplitude of the amplified entropy waves predicted by a linear analysis, [14,15], is 0.08690716 (shown in the following figures as horizontal solid lines). The pre-shock wave number, k, is selected such that $k \in \{13, 26\}$.

In order to get rid of the transient waves due to the initialization, the numerical procedure is defined so that the shock crosses the computational domain twice. The numerical solution is examined when the shock reaches $x = 4.5$ for the second time. For those computations, the CFL is lowered to the value 0.250.

First, for $k = 13$, and according to the spectral analysis above, we use 400 grid points that is effectively 10 points in each wavelength of the generated entropy wave. The results are shown in Fig. 13(a) (HENO2 monotonicity constraint) and Fig. 13(b) (Minmod constraint; the mean flow has been subtracted from the numerical solution).

We can see that the HLSM scheme – whatever the version considered – calculates the amplified entropy waves quite well, although their amplitude is still attenuated. On a grid of 800 points, Fig. 13(c) and (d), the resolution becomes very good. To compare, we produce the numerical results obtained with 1200 grid points, by using the HUWENO5 scheme, Fig. 13(e); obviously, the scheme produces excessive damping of the entropy waves: the reason is given by the non-linear weights that do not reach accurately their ideal values on such a grid. Lastly, Fig. 13(f) produces numerical results for $k = 26, N = 800$. Even if the amplitude of the entropy waves is slightly attenuated behind the shock, the HLSM scheme (HENO2 constraint) keeps on giving good results.

Example 5 (*Propagation of sound waves through a transonic nozzle [16]*). The computation of sound propagating through a choked nozzle presents a challenging problem for a shock-capturing scheme. To reduce the complexity of the problem, but retaining the basic physics and difficulties, this propagation problem is modelled by a one-dimensional acoustic wave transmission problem through a transonic nozzle [16].

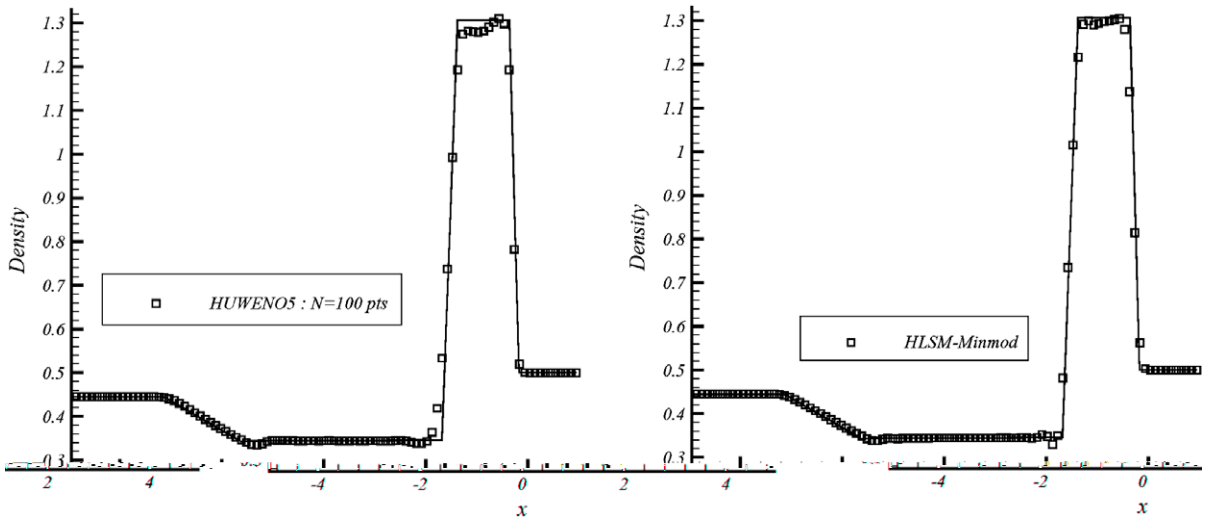

Fig. 11. The Lax problem. $N = 100$, $t = 1.30$, CFL $= 0.5$ Left: HUWENO5 scheme; right: HLSM–Minmod ($\alpha = 15$).

In this problem, an acoustic wave is introduced at the nozzle inflow region and the sound wave that travels downstream through the transonic nozzle and interacts with the shock is to be calculated. The amplitude of the incoming sound wave is $\varepsilon = 10^{-5}$, which is very small compared to the mean values of the flow. The nozzle flow is modelled by the one-dimensional Euler equations with variable nozzle area:

$$\begin{aligned} &\frac{\partial \mathbf{U}}{\partial t} + \frac{\partial \mathbf{F}(\mathbf{U})}{\partial x} = -\frac{1}{A}\frac{dA}{dx}\mathbf{U}' \\ &\mathbf{U} \equiv [\rho, \rho u, \rho E]^t, \quad \mathbf{F} \equiv [\rho u, \rho u^2 + p, \rho u H]^t, \quad \mathbf{U}' \equiv [\rho u, \rho u^2, \rho u H]^t \end{aligned} \tag{55}$$

The area of the nozzle is defined to be:

$$A(x) = \begin{cases} 0.536572 - 0.198086 \times \exp\left(-Log(2)\left(\frac{x}{0.6}\right)^2\right), & x > 0 \\ 1.0 - 0.661514 \times \exp\left(-Log(2)\left(\frac{x}{0.6}\right)^2\right), & x < 0 \end{cases}$$

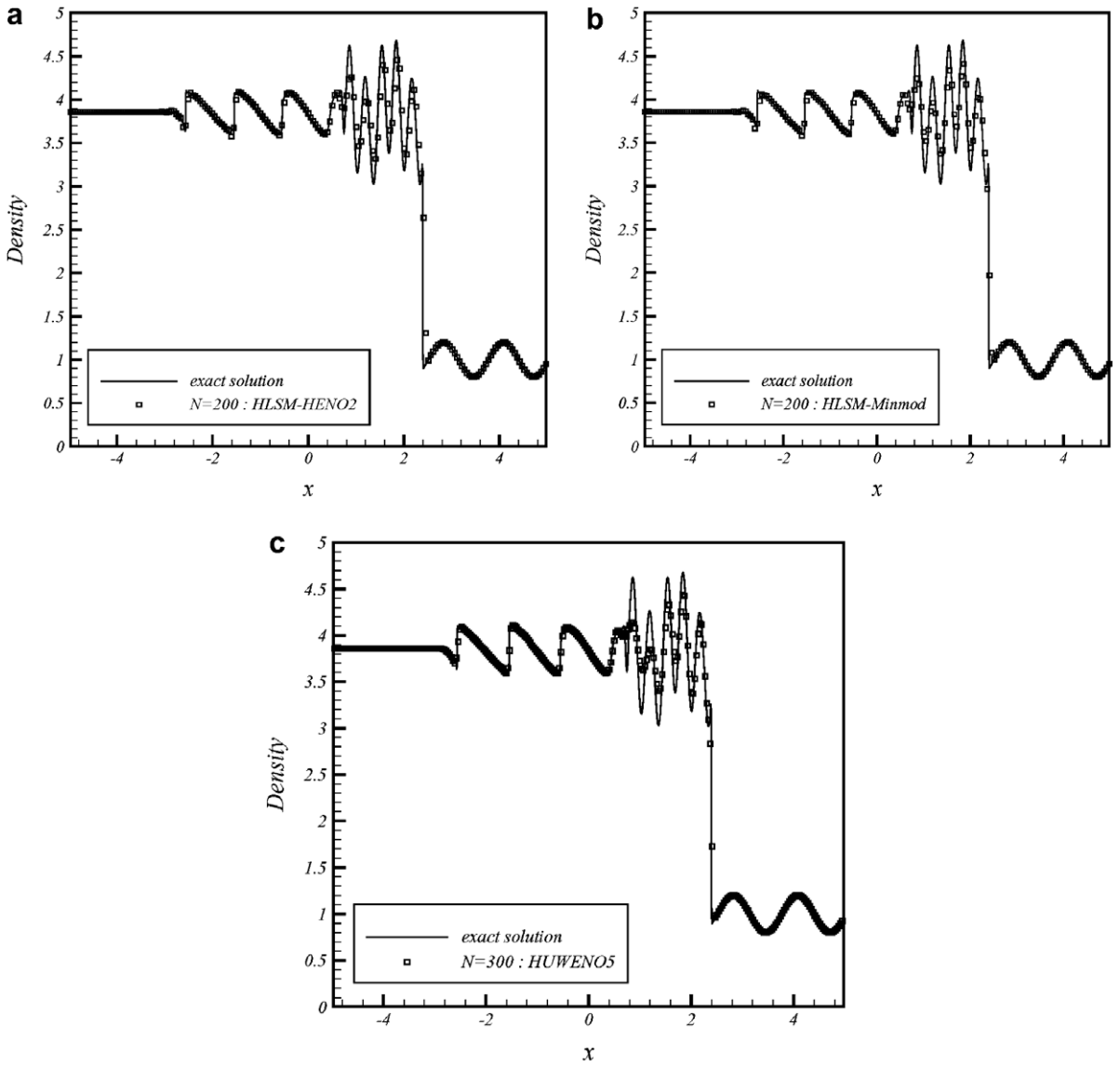

Fig. 12. The Shu–Osher problem. Density ρ. $t = 1.80$, CFL $= 0.8$. (a) HLSM–HENO2 ($N = 200$, $\alpha = 2$); (b) HLSM–Minmod ($N = 200, \alpha = 2$); (c) HUWENO5 scheme ($N = 300$).

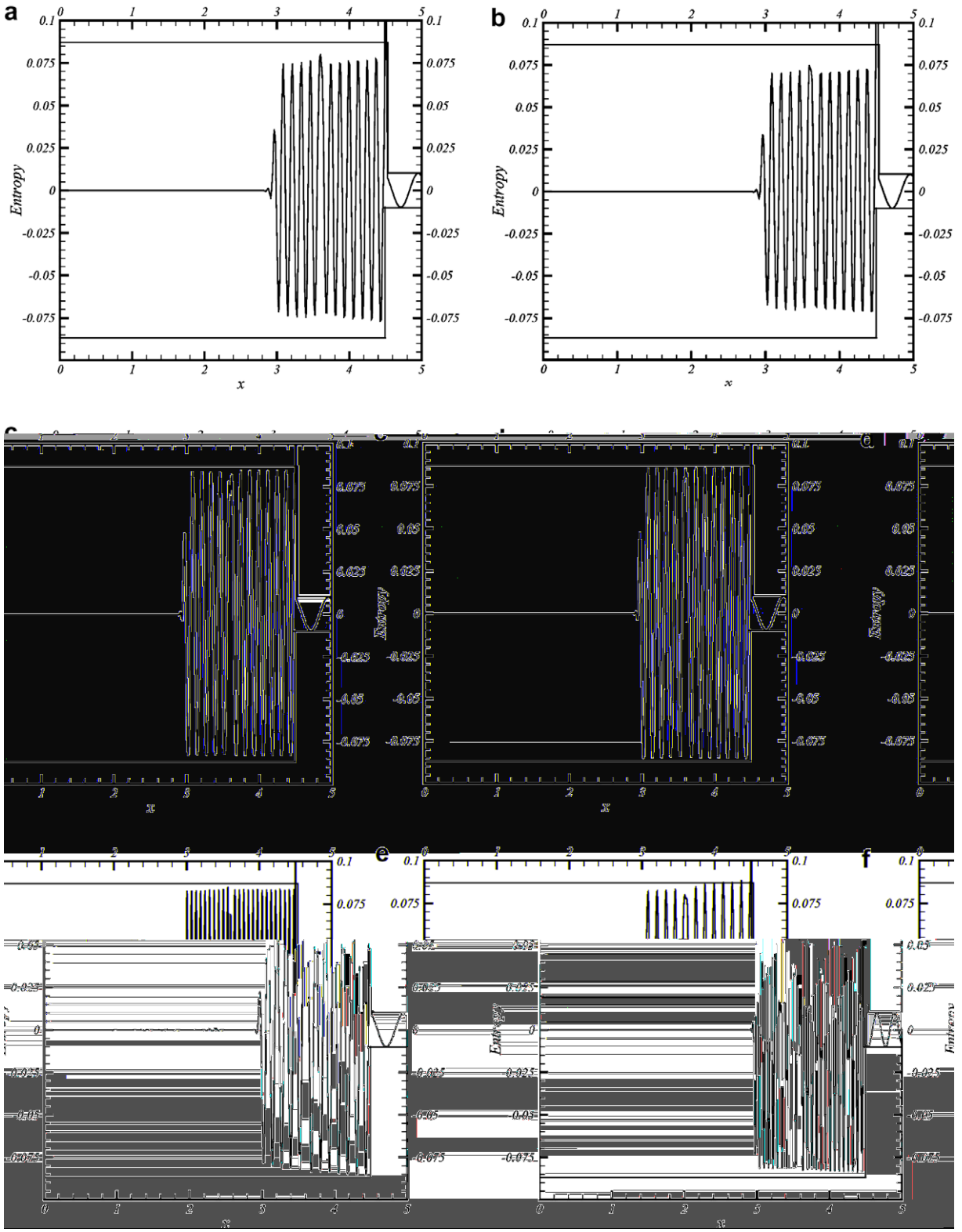

Fig. 13. Shock entropy wave interaction: $t = 2.2537,\ \alpha = 2,\ k = 13$. (a) HLSM–HENO2:$N = 400$; (b) HLSM–Minmod:$N = 400$; (c) HLSM–HENO2: $N = 800$; (d) HLSM–Minmod: $N = 800$ (e) HUWENO5: $N = 1200$; (f) HLSM–HENO2: $k = 26,\ N = 800$.

Flow variables are non-dimensionalized by using the upstream values. The velocity scale is a_∞ (speed of sound), the length scale is D (diameter of the nozzle) and the density scale is the static density, ρ_∞.

Then, the mean flow at the inlet is:

$$\begin{bmatrix} \bar{\rho} \\ \bar{u} \\ \bar{p} \end{bmatrix}_{inlet} = \begin{bmatrix} 1 \\ M_\infty \\ 1/\gamma \end{bmatrix} \tag{56}$$

The Mach number at the inlet, M_∞, is 0.2006533 and the pressure at the exit, p_{exit}, is 0.6071752, so that a shock is formed inside the nozzle. The shock location is then: $x_s = 0.3729$.

Just upstream of the shock wave, the Mach number is $M_1 = 1.465$ and downstream, $M_2 = 0.714$. The pressure ratio (intensity of the shock wave) is then $p_2/p_1 = 2.337$.

The incoming acoustic wave, with angular frequency, $\omega = 0.6\pi$, is described as:

$$\begin{bmatrix} \rho \\ u \\ p \end{bmatrix}_{acoustic} = \varepsilon \begin{bmatrix} 1 \\ 1 \\ 1 \end{bmatrix} \sin\left[\omega\left(\frac{x}{1+M_\infty} - t\right)\right] \tag{57}$$

The acoustic perturbations for the derivatives are derived from (57).

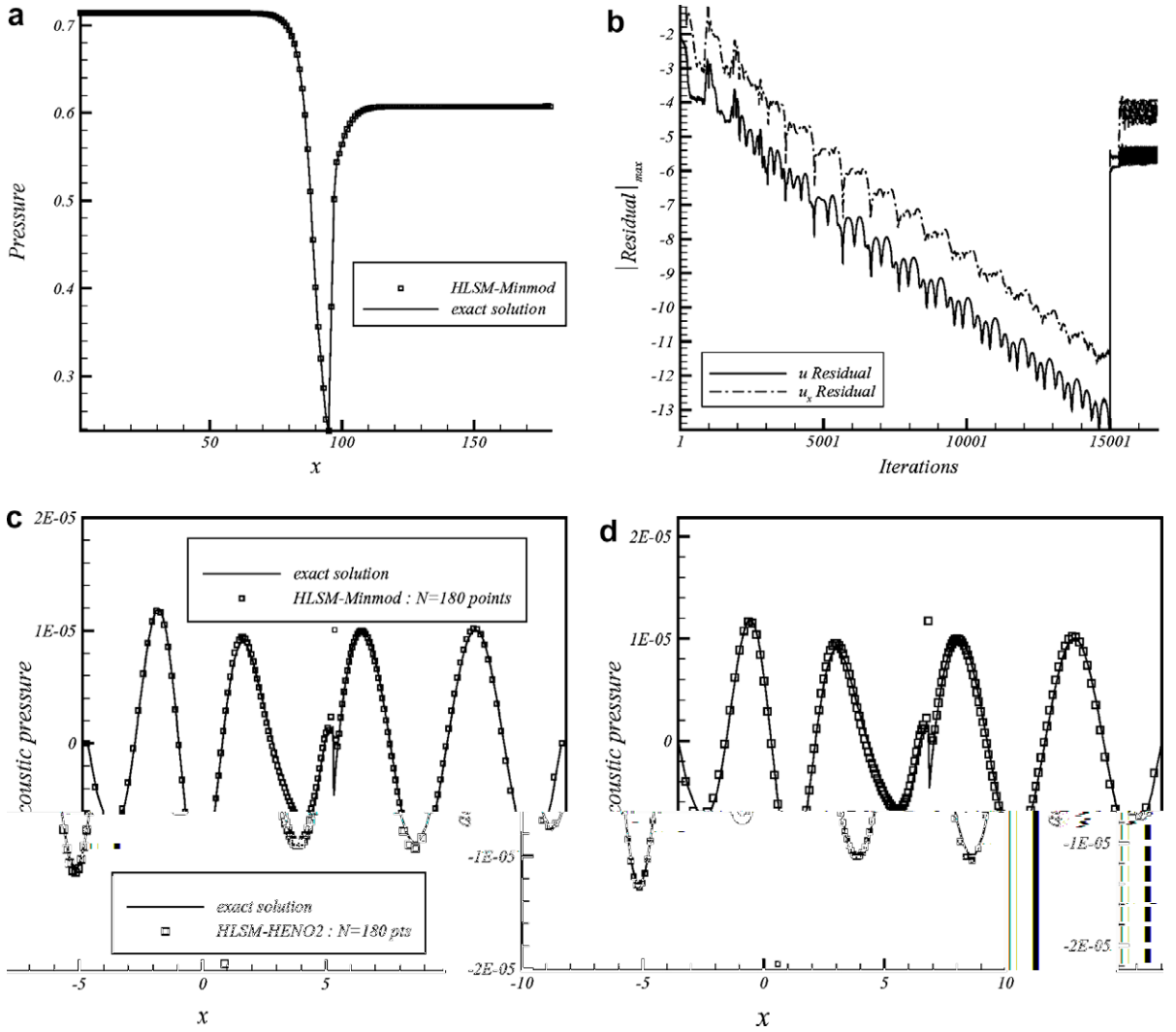

Fig. 14. Propagation of sound waves through a transonic nozzle. HLSM scheme: CFL = 0.8, $N = 180$, $\alpha = 2$, $\Delta x_{min}/\Delta x_{max} = 0.192$. (a) Steady-state solution: mean pressure, (b) maximum residual. (c) Acoustic pressure at $t = 14T$: HLSM–Minmod; (d) acoustic pressure: HLSM–HENO2.

In the present work, the acoustic wave will be computed directly by solving the non-linear governing equations rather than solving the linearized equations (see [16] for some examples on the linearized problem). This makes it harder to compute the acoustic waves. The challenge is whether the small amplitude wave can still be captured into the computation by the HLSM scheme. The computational domain is $-10 \leqslant x \leqslant 10$ and a non-uniform mesh, refined in the throat region, is used.

To begin, the steady state of the nozzle flow is computed. For the flow variables, the initial conditions are specified by using the mean exact solution of this problem.

The derivatives are then estimated by using a centred second-order finite-difference approximation. At the boundaries, the back-pressure is specified at the outlet and the total pressure and density are specified at the inlet. The other needed information at both the inlet and outlet, are obtained using extrapolation from their neighbouring mesh points. Concerning the derivatives, all those quantities are set to zero at the inlet since the flow is assumed uniform. At the outlet, the pressure derivative is set to zero while the remaining quantities are extrapolated in order for the error to leave the computational domain without numerical reflections.

The steady-state solution of (55), obtained using a 180 points non-uniform mesh ($\Delta x_{\min} = 6.74 \times 10^{-2}, \Delta x_{\max} = 0.35$) with CFL = 0.80, is compared with the exact solution, Fig. 14(a). The solution is converged to machine precision, Fig. 14(b). It can be seen that flow properties are uniform in most region of the nozzle, but change dramatically near the nozzle throat, Fig. 14(a). Lastly, the shock is captured without any numerical oscillation.

After the steady-state flow-field is computed, the acoustic wave propagation can be simulated using the same non-linear solver.

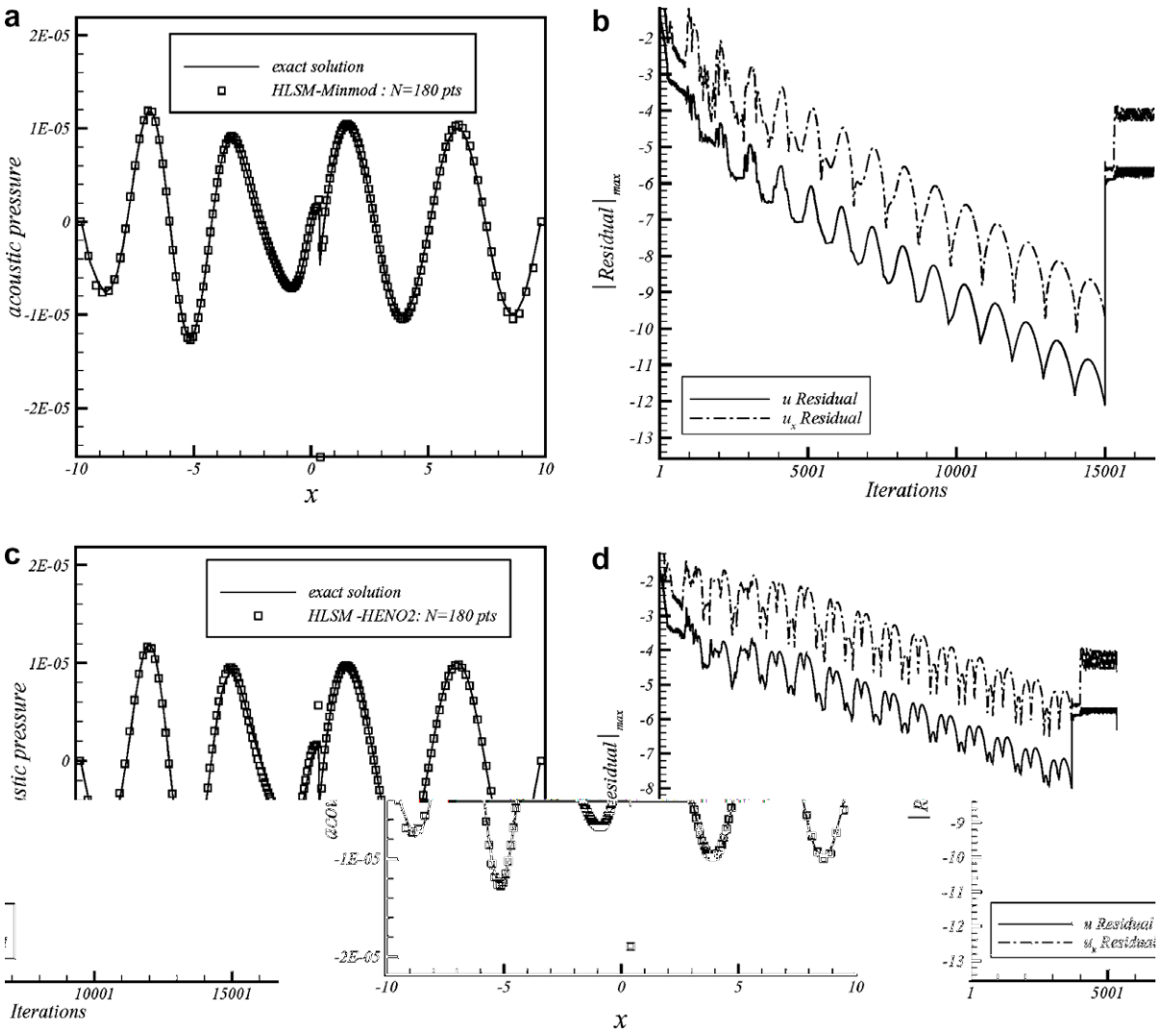

Fig. 15. Propagation of sound waves through a transonic nozzle. Acoustic pressure at $t = 14T$ HLSM scheme. (a, b) HLSM–Minmod: $\alpha = 10$; (c, d) HLSM–HENO2: $\alpha = 5$.

First, the initial conditions are specified using the steady-state solution previously calculated, then, at the inlet, the solution (57) is superimposed for the variables and its derivatives.

Numerical solutions of the acoustic pressure at $t = 14T$ are shown in Fig. 14(c) and (d) and compared with the analytical solution (given in [16]).

With $N = 180$ grid points, the wave pattern is correctly captured, either by the HLSM–HENO2 scheme, Fig. 14(c), or by the HLSM–Minmod scheme, Fig. 14(d).

However, the amplitude of the acoustic wave at the shock location is larger than that indicated by the analytical solution: this is due to a slight oscillation introduced by the scheme just at this place.

To improve these results, one can try to optimize the value of α for this particular test. Fig. 15 displays new numerical results obtained with $\alpha = 5$ (HLSM–HENO2, Fig. 15(c) and (d)) or $\alpha = 10$ (HLSM–Minmod, Fig. 15(a) and (b)). As one can see it, results are improved at the location of the discontinuity: the best results are obtained with the HLSM–Minmod version, Fig. 15(a). Concerning the HLSM–HENO2 scheme, a limiting cycle appears into the convergence process when α increases, Fig. 15(d): this limiting process prevents the convergence to a sufficiently low level and the acoustic fluctuations cannot be calculated anymore with a sufficient accuracy.

In spite of this difficulty, one can note that the profiles of the acoustic pressure both upstream and downstream the shock location, agree very well with the analytical solution, Figs. 14 and 15.

As it is known, any high-order scheme captures the shock with a first-order accuracy [13]; however, those results demonstrate that this defect does not alter the smooth part of the solution: the multi-scale structure of the solution is preserved after having crossed the shock wave. In other words, this result means that the numerical error generated by capturing the shock remains confined and does not propagate. Thus, this property explains the good results obtained with the HLSM scheme. The main advantage of such a scheme comes from its compactness and the definition of its non-linear weight, w_i, defined to modulate the monotonicity constraints: this enables to generate a local first-order correction when a discontinuity appears.

5. Concluding remarks

In this paper, we constructed a new Hermite least-square interpolation (HLSM) for 1D hyperbolic conservation laws. This new technique is aimed to deal with irregular meshes while preserving high-order accuracy.

When the solution is smooth, this procedure generates a fifth-order spatial accuracy. In regions of discontinuities, two additional numerical constraints are introduced into the Hermite least-square system. These constraints impose that the high-order reconstruction locally coincides with a low-order monotone reconstruction. To emulate those monotonicity constraints only in regions of non-smooth data, we developed a data-depending weight. According to the magnitude of this weight, the monotonicity constraints either are discarded (the resulting scheme is fifth-order accurate) or emphasized (the scheme locally behaves as a first-order scheme).

In addition, we introduced into the definition of this weight, a parameter that we called the "monotonicity parameter". This parameter is aimed to monitor the numerical dissipation at the location of a discontinuity. Accuracy and spectral analysis combined with numerical investigations gave us the following significant results:

- In regions of discontinuities, the spatial truncature error becomes first-order, resulting in a monotone behaviour of the scheme. Increasing the monotonicity parameter results in an increase of the numerical dissipation of the scheme. However, this dissipative term is bounded by that of an upwind first-order scheme.
- When the solution is smooth, the monotonicity parameter has no influence on the accuracy of the scheme.
- The specific form of the monotonicity constraints is significant only on coarse meshes. In such a case, an ENO constraint is desirable.
- The way of initializing the first-derivative has no influence neither on the accuracy of the scheme nor on its stability.
- On irregular meshes, the scheme efficiently calculates multi-scale problems without generating too much numerical dissipation.

Considering those results, the HLSM method seems to perform reasonably well – at least for the numerical problems investigated. In a next future, we shall develop a HLL Riemann solver that will be more suited for a Hermite formulation. In that case, the benefit hoped is an improvement of the handling of contact discontinuities or strong expansions.

Acknowledgment

The author wishes to thanks with recognition, Dr. G.B. Deng (Ecole Centrale de Nantes – France) who provided all technical support essential to this work.

Appendix. Spectral analysis for the HLSM scheme

This study required the intensive use of the MAPLE symbolic mathematical computer package.

We start this analysis from the linear semi-discrete form (47):

$$\left.\frac{dU}{dt}\right|_i + a\frac{U^L_{i+1/2} - U^L_{i-1/2}}{\Delta x} = 0 \tag{A1}$$

This form is supposed to be the discretized form, by the HLSM method, of Eq. (46). Now, assuming that the calculation domain is periodic, we decompose the discrete vector solution, $U_i \equiv (\bar{u}_i, \bar{r}_i)^t$, in Fourier series:

$$U_i = \widehat{U} \times e^{jkx_i} (j^2 = -1) \tag{A2}$$

where $\widehat{U} \equiv (\hat{u}, \hat{r})^t$ represents the complex amplitude of the vector solution and k, the wave number of the periodic signal.

Inserting (A2) into (A1) produces the following result:

$$\frac{d\widehat{U}}{dt} = G(\beta, v, \alpha) \times \widehat{U} \tag{A3}$$

$G(\beta, v, \alpha)$ is a complex 2×2 matrix that represents the discrete Fourier transform of the spatial operator in (A1). This matrix only depends upon the phase angle, β ($\equiv k\Delta x$), the CFL number, v ($\equiv a\Delta t/\Delta x$) and the "monotonicity parameter", α.

To explicitly formulate $G(\beta, v, \alpha)$, we need to develop the characteristics of the HLSM scheme.

Thus, the HLSM reconstruction necessitates inverting the following 6×4 linear least-square problem (Eq. (19) modified by (26)):

$$L \times A = B \tag{A4}$$

with $L \equiv [L_j]^t_{j\in\{1,\ldots,6\}}$: metric terms (modified by w_i for $L_{5,6}$); $A \equiv \left[\{\tilde{a}_j\}_{j\in\{1,2,3,4\}}\right]^t$: polynomial coefficients; $B \equiv [\bar{u}_{i-1} - \bar{u}_i, \bar{u}_{i+1} - \bar{u}, \bar{r}_{i-1} - \bar{r}_i, \bar{r}_{i+1} - \bar{r}, w_i \times B_5, -w_i \times B_5]^t$: numerical constraints.

To get an analytical solution for A, system (A4) is partially inverted via a Gram–Schmidt process. This way, system (A4) becomes:

$$R \times A = Q^t \times B \tag{A5}$$

where Q is a symmetric and orthogonal 6×6 matrix resulting from the $L = Q \times R$ decomposition; R is an upper-triangular 4×6 matrix. Both matrices only depend upon the metric terms identified by Eq. (12). The monotonicity parameter, α, explicitly appears in those terms through the introduction of the weight, w_i.

Therefore, inserting (A2) into (A5), the resulting system can be explicitly solved for the vector $\widehat{A} \equiv [\{\hat{a}_j\}_{j\in\{1,2,3,4\}}]^t$, which now represents the Fourier transform of the initial vector, A ($\{\hat{a}_j\} \equiv$ Fourier transform of the space derivatives, $\{a_j\}$).

Thus, we get in the Fourier space the following result:

$$\widehat{A} = \mathcal{L}(\beta, \alpha) \times \widehat{U}(\beta \equiv k \times \Delta x) \tag{A6}$$

Then, it becomes possible to evaluate the Fourier transform of the interpolated values $(u^L_{i+1/2}, r^L_{i+1/2})$:

$$\begin{cases} \hat{u}^L_{i+1/2} = \left(\hat{u} + \hat{a}_1\frac{\Delta x}{2} + \hat{a}_2\frac{\Delta x^2}{6} + \hat{a}_3\frac{\Delta x^3}{8} + \hat{a}_4\frac{\Delta x^4}{20}\right) \times e^{jkx_i} \\ \hat{r}^L_{i+1/2} = \left(\hat{r} + \hat{a}_2\Delta x + \hat{a}_3\frac{\Delta x^2}{2} + \hat{a}_4\frac{\Delta x^3}{2}\right) \times e^{jkx_i} \end{cases} \tag{A7}$$

Consequently, evaluating the expression: $a\Delta t \times \frac{\widehat{U}^L_{i+1/2} - \widehat{U}^L_{i-1/2}}{\Delta x}$, one can explicitly formulate the complex matrix, $G(\beta, v, \alpha)$, in (A3); this matrix is too complicated to be given in this paper.

Finally, integrating (A3) by the third-order TVD Runge–Kutta scheme,[12], over the interval $[t_n, t_{n+1}]$, produces the following result:

$$\widehat{U}^{n+1} = \mathcal{G}(\beta, v, \alpha) \times \widehat{U}^n \tag{A8}$$

where: $\mathcal{G}(\beta, v, \alpha) \equiv \left[Id + G \times \left[Id + \frac{1}{2}G \times \left[Id + \frac{1}{3}G\right]\right]\right]$ is a 2×2 complex matrix; Id represents the 2×2 identity matrix.

$\mathcal{G}(\beta, v, \alpha)$ is called the "amplification matrix" of the scheme and makes it possible to analyze the numerical properties of the HLSM discretization.

For this purpose, the exact amplification matrix for (46) must be specified. Using a continuous Fourier transform of (46), we get the differential form:

$$\frac{d\widehat{U}}{dt} + jka \times \widehat{U}(t) = 0 \tag{A9}$$

Integrating, exactly, this form between t_n and t_{n+1}, we obtain:

$$\widehat{U}^{n+1} = e^{-jv\beta} \times \widehat{U}^n \tag{A10}$$

Specifically, if $U(x, t = 0) = [\cos kx, -k \sin kx]^t$, then the relation that follows can be obtained from (A10):

$$\widehat{U}^{n+1} = \begin{bmatrix} 1 \\ \frac{j\beta}{\Delta x} \end{bmatrix} \times e^{-j(n+1)v\beta} \tag{A11}$$

From this result, we can identify the following quantities:

$$\begin{cases} r_e(\beta) \equiv [1, j\beta/\Delta x]^t \\ \lambda_e(\beta, v) \equiv e^{-jv\beta} \\ \hat{w}_e(\beta, v) \equiv 1 \end{cases} \tag{A12}$$

$\lambda_e(\beta, v)$ represents the exact eigenvalue of system (46), $r_e(\beta)$ is its associated eigenvector while $\hat{w}_e(\beta, v)$ represents the complex amplitude of the exact solution.

Now, returning to the amplification matrix, $\mathcal{G}(\beta, v, \alpha)$, we can calculate its eigenvalues: $\lambda_1(\beta, v, \alpha)$ and $\lambda_2(\beta, v, \alpha)$.

Defining $\Lambda \equiv diag[\lambda_1, \lambda_2]$, one can also write: $\mathcal{G} \equiv \mathcal{R}\Lambda\mathcal{R}^{-1}$; where the matrix $\mathcal{R}$ is defined as the matrix of the right eigenvectors of $\mathcal{G}(\beta, v, \alpha) : \mathcal{R} \equiv [r_1(\beta, v), r_2(\beta, v)]^t$.

Finally, by defining $\widehat{W} \equiv [\hat{w}_1, \hat{w}_2]^t \equiv \mathcal{R}^{-1} \times \widehat{U}$ and inserting this definition into relation (A8), one obtains by recurrence:

$$\widehat{U}^{n+1} = \lambda_1^{n+1}\hat{w}_1^0\hat{r}_1 + \lambda_2^{n+1}\hat{w}_2^0\hat{r}_2 \tag{A13}$$

By definition, the first component of the right-hand term is called the "accurate component" of the numerical solution. In other words, if we compare (A11) with (A13), the quantity $\lambda_1^{n+1}\hat{w}_1^0\hat{r}_1$ represents the approximation of the quantity $[1, j\beta/\Delta x]^t \times e^{-j(n+1)v\beta}$. More precisely, using (A12) we can specify the following approximations:

$$\begin{cases} \lambda_1(\beta, v, \alpha) \sim e^{-jv\beta} \\ r_1(\beta, v, \alpha) \sim [1, j\beta/\Delta x]^t \\ \hat{w}_1(\beta, v, \alpha) \sim 1 \end{cases} \tag{A14}$$

Practically, the "accurate eigenvalue", $\lambda_1(\beta, v, \alpha)$, is identified from $\mathcal{G}(\beta, v, \alpha)$ by using the consistency condition:

$$\lambda_1(\beta, v, \alpha) \underset{\beta \to 0}{\to} 1 \tag{A15}$$

Then, its associated eigenvector, $r_1(\beta, v, \alpha)$, can be evaluated. $\hat{w}_1^0$, which represents the complex amplitude at $t = 0$, of the accurate component of the solution, is calculated from the initial conditions for $\widehat{U}^0$.

For example, if $U(x, t = 0) \equiv [\cos kx, -k \sin kx]^t$ and if this initial condition is approximated by a second-order centred discretization, then we get the result:

$$\widehat{U}^0 = [1, j \sin \beta/\Delta x]^t \tag{A16}$$

Therefore, by writing (A13) at $t = 0$, we obtain the relation:

$$\widehat{U}^0 = \hat{w}_1^0 r_1 + \hat{w}_2^0 r_2 \tag{A17}$$

By using (A16), system (A17) is easily inverted to determine $\hat{w}_{1,2}$.

By contrast, the remaining component in the right-hand side of (A13) is called the "spurious component" of the numerical solution. This component is a general characteristic of extended algebraic systems that use auxiliary variables – in our case, the first-derivative of the solution – and has no counterpart in the differential problem. This component represents the behaviour of the numerical error introduced either at the boundaries or at $t = 0$, by the approximation of the first derivative; it can also be excited on highly distorted meshes.

The spurious component of the numerical solution must be damped in time, whatever the mesh, so that the accurate part of the solution is not affected. For a more detailed explanation about the notion of "spurious component" and its behaviour, we refer the interested reader to [1].

Finally, knowing the analytical form of $\mathcal{G}(\beta, v, \alpha)$, the spectral analysis of the HLSM scheme can be fully managed by defining the following quantities:

- the discretization error at $t = t_n$: $\left|e^{-jnv\beta} - \lambda_1^n\hat{w}_1^0 r_1\right|$
- the spurious error at $t = t_n$: $\left|\lambda_2^n\hat{w}_2^0 r_2\right|$
- the truncature error (space and time): $\left|e^{-jv\beta} - \lambda_1\right|/\beta$
- the amplitude error: $1 - |\lambda_1|$
- the phase error: $|1 + Arg(\lambda_1)/v\beta|$

Those quantities are parameterized by the number of cells-per-wavelength, N ($N \times \beta = 2\pi$), the CFL number, v and the monotonicity parameter, α.

References

[1] B. Van-Leer, Towards the ultimate conservative difference scheme III A new approach to numerical convection, J. Comput. Phys. 23 (1977) 276–299.
[2] A. Harten, B. Engquist, S. Osher, S. Chakravarthy, Uniformly high-order essentially non-oscillatory schemes III, J. Comput. Phys. 71 (1987) 231–303.
[3] X.-D. Liu, S. Osher, T. Chan, Weighted essentially non-oscillatory schemes, J. Comput. Phys. 115 (1994) 200–212.
[4] C-W. Shu, Essentially non-oscillatory and weighted essentially non-oscillatory schemes for hyperbolic conservation laws, ICASE Report 97-65, 1997.
[5] G. Capdeville, A Hermite upwind WENO scheme for solving hyperbolic conservation laws, J. Comput. Phys. 227 (2008) 2430–2454.
[6] T.J. Barth, Aspects of unstructured grids and finite-volume solvers for the Euler and Navier–Stokes equations, VKI Lecture Series, 1994–05.
[7] T.J. Barth, Recent developments in high-order k-exact reconstruction on unstructured meshes, AIAA Paper 93-0668, January 1993.
[8] C.F.O. Gooch, Quasi-ENO schemes for unstructured meshes based on unlimited data-dependent least-squares reconstruction, J. Comput. Phys. 133 (1997) 6–17.
[9] B. Einfeldt, C.D. Munz, P.L. Roe, B. Sjögreen, On Godunov-type methods near low densities, J. Comput. Phys. 92 (1991) 273–295.
[11] J. Qiu, C-W. Shu, Hermite WENO schemes and their applications as limiters for Runge–Kutta discontinuous Galerkin method: one-dimensional case, J. Comput. Phys. 193 (2004) 115–135.
[12] C.-W. Shu, S. Osher, Efficient implementation of essentially non-oscillatory shock-capturing schemes, J. Comput. Phys. 77 (1988) 439–471.
[13] R.G. Hindman, On shock-capturing methods and why they work, AIAA-Paper-88-0622.
[14] J. Mc Kenzie, K. Westphal, Interaction of linear waves with oblique shock waves, Phys. Fluids 11 (1968) 2350–2362.
[15] T.A. Zang, M.Y. Hussaini, D.M. Bushnell, Numerical computations of turbulence amplification in shock wave interactions, AIAA J. 22 (1984) 13–21.
[16] Third computational aeroacoustics workshop on benchmark problems, NASA/CP-2000-209790.
[17] J. Qiu, C-W. Shu, On the construction comparison and local characteristic decomposition for high-order central WENO schemes, J. Comput. Phys. 183 (2002) 187–209.
[18] V.M. Shelkovitch, The Riemann problem admitting δ-, δ'-shocks and vacuum states (the vanishing viscosity approach), J. Differ. Eqaut. 231 (2006) 459–500.
[19] Y. Liu, Central schemes on overlapping cells, J. Comput. Phys. 209 (2005) 82–104.
[20] S. Li, F. Xiao, A semi-Lagrangian characteristic formulation, J. Comput. Phys. 222 (2007) 849–871.